Experimental Constraints on the Origin of the Lunar High-Ti Basalts

C P Haupt, C J Renggli, A Rohrbach, J Berndt, S Klemme

JGR Planets

RESEARCH ARTICLE

10.1029/2023JE008239

Experimental Constraints on the Origin of the Lunar High-Ti Basalts

C. P. Haupt[1,2], C. J. Renggli[1,3], A. Rohrbach[1], J. Berndt[1], and S. Klemme[1]

[1]Institut für Mineralogie, Universität Münster, Münster, Germany, [2]CNRS, Université d'Orléans, Orléans, France, [3]Max-Planck-Institute for Solar System Research, Göttingen, Germany

Key Points:

- High-Ti lunar basalts can be produced experimentally by a simple melting process of a hybrid lunar cumulate mantle with nonmodal ilmenite/clinopyroxene
- The entire chemical spectrum of most primitive lunar basalts requires additional processes such as reactive ascent and assimilation
- The process of partially melting a heterogeneous lunar mantle also yields melts with similarities to low-Ti, high-Al lunar mare basalts

Correspondence to:

C. P. Haupt,
chaupt1@uni-muenster.de

Citation:

Haupt, C. P., Renggli, C. J., Rohrbach, A., Berndt, J., & Klemme, S. (2024). Experimental constraints on the origin of the lunar high-Ti basalts. *Journal of Geophysical Research: Planets*, *129*, e2023JE008239. https://doi.org/10.1029/2023JE008239

Received 9 DEC 2023
Accepted 11 JUL 2024

Author Contributions:

Conceptualization: C. P. Haupt
Data curation: C. P. Haupt, J. Berndt
Formal analysis: C. P. Haupt, J. Berndt
Funding acquisition: A. Rohrbach, S. Klemme
Investigation: C. P. Haupt, C. J. Renggli
Methodology: C. P. Haupt, C. J. Renggli, S. Klemme
Project administration: S. Klemme
Resources: A. Rohrbach, J. Berndt
Software: C. P. Haupt
Supervision: C. J. Renggli, A. Rohrbach, S. Klemme
Validation: J. Berndt
Visualization: C. P. Haupt
Writing – original draft: C. P. Haupt
Writing – review & editing: C. J. Renggli, A. Rohrbach, S. Klemme

Abstract High-pressure and high-temperature experiments were conducted to simulate melting of a hybrid cumulate lunar mantle. The experimental results show that intermediate to high-Ti lunar pyroclastic glasses (>6 wt% TiO_2) can be produced by partial melting of lunar cumulates. High-Ti basalts are generated when the ilmenite/clinopyroxene ratios in the lunar mantle cumulates are between 1/1 and 4/1, depending on the degree of melting. The presence of an urKREEP component in the mantle cumulate strongly influences Al_2O_3/CaO of the melts. The experiments provide strong evidence for the model that the compositional diversity of lunar basalts is a consequence of a gravitational overturn of the lunar interior after the lunar magma ocean had solidified. Ilmenite/clinopyroxene in the cumulate mantle, which generates high-Ti melts at partial melting, do not comprise the ratios in ilmenite-bearing cumulates (IBC), which crystallized after ∼90% solidification of the lunar magma ocean and indicate local accumulation of ilmenite in the overturned lunar mantle. However, to fully match the natural composition of the most primitive lunar samples, secondary processes such as assimilation are still required.

Plain Language Summary The basalt samples, which were returned from the Earth's Moon by astronauts during sample return missions, are chemically different from terrestrial basalts. Whilst terrestrial basalts usually contain less than 1 wt% of TiO_2, the lunar rocks can contain more than >6 wt% of TiO_2. The origin of these extraordinarily high TiO_2 contents has long been debated, and hence we conducted experiments at high pressures and temperatures to simulate melting of a heterogeneous lunar mantle. Our experimental results imply that the lunar high-Ti basalts can be produced by melting of a heterogeneous lunar mantle that contains high amounts of Ti-rich minerals, such as ilmenite or similar Fe and Ti-rich oxides, and silicate minerals, such as olivine, orthopyroxene, and clinopyroxenes. Our results support the hypothesis that the stratification of the lunar mantle after it had solidified was not preserved, suggesting a high dgree of heterogeneity within the mantle. Besides Ti, other major elements of our melts do not completely match the natural samples. This can be accounted for by interaction with the host rocks during the ascent of the magmas.

1. Introduction

The compositional variety of lunar mare basalts and pyroclastic glasses sampled during the Apollo and Luna missions (Neal & Taylor, 1992; Shearer et al., 2006), and the recent Chinese Chang'E-5 sample return mission (Fu et al., 2022) indicates a complex and heterogeneous nature of the lunar mantle. The diversity of lunar basalts and volcanic glasses is reflected in the range of TiO_2 contents, which has been used to classify mare basalts into very low Ti (VLT) basalts (<1 wt% TiO_2), low-Ti basalts (1–6 wt% TiO_2), intermediate basalts (5–9 wt% TiO_2), and high-Ti basalts (9–14 wt% TiO_2) (Papike & Vaniman, 1978). The variable Ti content corresponds to color in the pyroclastic glasses, ranging from green (VLT) over yellow toward orange (high-Ti) and red/black (>12 wt% TiO_2, Delano, 1986).

The chemical diversity of lunar mare basalts cannot be explained by simple peridotite melting and/or mineral fractionation processes (Longhi, 1992; Ringwood & Essene, 1970). Consequently, two more complex models have been proposed to explain the origin of the high-Ti basalts:

(I) High-Ti contents of lunar basalts are the result of shallow assimilation of high-Ti oxides by low-Ti mantle melts, the latter of which are formed by melting of harzburgite deep in the lunar interior (Barr & Grove, 2013; Finnila et al., 1994; Hubbard & Minear, 1975; Wagner & Grove, 1997).
(II) High-Ti lunar magmas are partial melts derived from a heterogeneous lunar interior, originating from a mixed harzburgite and ilmenite-pyroxenitic source, after the original stratification of the solidified lunar

magma ocean (LMO) had gravitationally collapsed (Kommescher et al., 2020; Ringwood & Kesson, 1976; Shearer & Papike, 1999; Singletary & Grove, 2008; Snyder et al., 1992).

Both models acknowledge that the lunar interior is the consequence of an LMO, which crystallized into layers upon its solidification. Olivine and orthopyroxene crystallized first (until ∼60–70% LMO solidification), followed by plagioclase (Charlier et al., 2018; Elkins-Tanton et al., 2011; Rapp & Draper, 2018; Schmidt & Kraettli, 2022). Plagioclase buoyantly segregated and floated upward to form the primary lunar anorthosite crust (Papike et al., 1997; Solomon & Nafi Toksöz, 1973; Warren, 1985). The remaining melt crystallized low- and high-Ca pyroxene, and finally dense Fe-Ti oxides on top of the less dense harzburgite (3,700 kg/m³ and 3,400 kg/m³, respectively; Hess & Parmentier, 1995). This late stage Fe-Ti enriched layer is often abbreviated as IBC, which is short for "Ilmenite-bearing-cumulate" in lunar petrology (Hess & Parmentier, 1995). On top of it the last drags of melt crystallized, which contain high concentrations of very incompatible elements and are therefore referred to as urKREEP (highlighting high concentrations in potassium (K), the rare earth elements (REE) and phosphorous (P)). Geodynamic models indicate that the density contrast between the IBC and the harzburgite mantle (Hess & Parmentier, 1995; Ringwood & Kesson, 1976; Spera, 1992) caused a large-scale LMO overturn, which induced chemical heterogeneities into the lunar mantle. Furthermore, recent geodynamic studies have proposed that the lateral distribution of IBC in the Moon is heterogeneous (Khan et al., 2014; Xu et al., 2022). Additionally, KREEP-rich material could have been dragged along down into the lunar mantle during overturn, which may have redistributed heat-producing elements in the lunar interior (Khan et al., 2014; Shearer et al., 1991). The chemically and mineralogically heterogeneous lunar mantle that results from the overturn is often referred to as "hybridized" lunar mantle (Elkins et al., 2000; Ringwood et al., 1972; Snyder et al., 1992; Spera, 1992). The precise chemical and mineralogical composition of this mantle, along with the composition of ilmenite-bearing cumulate layers, remains poorly constrained.

Dissolution experiments of ilmenite and diopside by high- and low-Ti picritic lunar magmas, testing model I, successfully produced high-Ti melts, suggesting an ilmenite/high-Ca pyroxene (ilm/cpx) in the IBC cumulate of 2/1 (Van Orman & Grove, 2000; Wagner & Grove, 1997). Magma ocean crystallization models, however, result in an ilm/cpx of 1/3–1/6 (Charlier et al., 2018; Rapp & Draper, 2018; Schmidt & Kraettli, 2022; Snyder et al., 1992). This observation deems the assimilation of unaltered IBC by low-Ti basaltic melts unlikely. Model II, melting of a heterogeneous hybridized lunar mantle, was simulated by several experimental studies, but experimental melt compositions do not cover the entire range (5–16.4 wt% TiO_2) of the intermediate to high-Ti basalts (Mallik et al., 2019; Singletary & Grove, 2008; Thacker et al., 2009). Several studies investigated melting of a pure IBC layer (Mallik et al., 2019; Van Orman & Grove, 2000), resulting in either too low contents of TiO_2 (∼10 wt%) or adequately high contents of TiO_2 but too high CaO/Al_2O_3. In fact, pure IBC melting will always produce melts with CaO contents higher than those of picritic basalt samples (Mallik et al., 2019). On the other hand, mixing of harzburgite with only Fe-Ti oxides, such as ilmenite and armalcolite, results in melts with too high TiO_2 (>20 wt%) and MgO >18 wt% (Thacker et al., 2009). Hence, a cumulate with the potential to produce picritic basalt compositions by simple melting must contain a harzburgite component, as well as ilmenite and significant proportions of clinopyroxene. Only a few attempts addressed the potential of a hybrid lunar mantle containing variable amounts of an olivine + orthopyroxene mantle and a high-Ti component (i.e., IBC with ilmenite + clinopyroxene) ± KREEP to create high-Ti picritic basalt compositions by simple melting (Brown & Grove, 2015; Singletary & Grove, 2008). Those studies revealed that it is indeed plausible to generate yellow and orange picritic glasses ranging between 7 and 10 wt% of TiO_2.

These studies showed that the composition of the IBC layer largely controls the composition of partial melts (Singletary & Grove, 2008). As pointed out earlier, depending on the exact model constrains, the ratio of ilm/cpx in the last crystallizing fraction of the LMO diverges significantly (1/6 up to 2/1). Furthermore, it is assumed that layering during cumulate formation might not preserve the modal proportions of the crystallizing phases (Brown & Grove, 2015; McCallum et al., 1980). This could result in a local accumulation of ilmenite due to the fact that ilmenite is denser than pyroxene. Hence, we assume small scale heterogeneities inside the IBC layer, where modal proportions (∼1/6 after fractional crystallization of the LMO, Charlier et al., 2018) are not preserved. This was also suggested by Singletary and Grove (2008), who hypothesized that a modally variable residue could create observed variations in the lunar ultramafic glasses. Considering the mantle heterogeneities arising from the overturn in the later stages of the LMO, our objective is to experimentally validate hypothesis II and further explore the effects of modally variable cumulate compositions. This involves a systematic investigation of the range of melts that can be produced through partial melting of a highly heterogeneous, hybridized lunar mantle

(Ringwood & Kesson, 1976). Our emphasis is on replicating high-Ti compositions and expanding the possible melt compositions resulting from melting a hybrid lunar mantle. This will allow the investigation of the source composition of the most primitive lunar mantle melts (Delano, 1986).

To constrain the influence of mineralogy and chemical composition of cumulates on partial melt compositions, we prepared a range of cumulate compositions with and without a fixed KREEP component, as introduced by Warren and Wasson (1979). We ran conventional high-temperature high-pressure experiments at temperatures between 1,250 and 1,500°C. Most experiments were conducted at 1.5 GPa, which corresponds to the lower limit of the source depth of most primitive lunar basalts between 250 and 500 km (Delano, 1980; Elkins-Tanton et al., 2003, 2004, 2011; Green et al., 1975; Guenther et al., 2022; van Kan Parker et al., 2011) and to the depth of the lunar mantle, where high-Ti lunar melt are supposed to be positively buoyant (Elkins-Tanton et al., 2002; Singletary & Grove, 2008).

2. Materials and Methods

2.1. Starting Material Compositions

The starting material compositions CMV, CMVI, and CMVI_II were designed using fixed lunar cumulate compositions, similar to the work done by Singletary and Grove (2008). The main cumulate component in CMV, CMVI, and CMVI_II is a harzburgite lunar mantle cumulate (Hess & Parmentier, 1995; Singletary & Grove, 2008), which resembles Hess and Parmentier (1995)'s constrained early mantle cumulate (harzburgite with 1:1 olivine (ol) and orthopyroxene (opx), Table 1). A minor fixed component in CMV, CMVI, and CMVI_II comprises an urKREEP-cumulate with a major element composition following Warren and Wasson (1979), comprising plagioclase (52 wt%), orthopyroxene (30 wt%), and minor amounts of olivine (10 wt%), clinopyroxene (cpx: 7 wt%), and ilmenite (~1 wt%). The fixed KREEP layer composition was used only to mix CMV, VI, and VI_II. The third component in these starting materials is a late stage cumulate (IBC) comprising ilmenite, clinopyroxene, and small amounts of plagioclase. The ilm/cpx ratios in CMV, CMVI, and CMVI_II were altered by mixing variable amounts of clinopyroxene, ilmenite, and plagioclase. The mineral compositions were obtained from the last crystallization step of the LPUM bulk silicate Moon composition (Longhi, 2006) at 1,040°C (Charlier et al., 2018). To investigate the consequences of nonmodal ilm/cpx in the IBC, we chose relatively high proportions in the starting mix CMV (4/1), similar to what has been proposed based on assimilation experiments (Wagner & Grove, 1997). In starting material CMVI and VI_II, we added plagioclase and reduced ilm/cpx to 1/7 in order to investigate the lower extreme.

Experiments on starting materials CMV, CMVI, and CMVI_II have elevated TiO_2 but do not match Al_2O_3/CaO with elevated Al_2O_3 compared to picritic melt compositions. We attribute this to the urKREEP component, which is plagioclase-rich. Additional starting materials (CMX, X_II, XI, and XV) have a modified mineralogy of the IBC component as well as a different harzburgite mantle composition.

Olivine and orthopyroxene major element compositions from CMV (ID GPC_769) were taken to mix the harzburgite component in CMX, X_II, XI, and XV. In CMX and X_II, the harzburgite component comprises ol/opx of 11/9, whereas in CMXI and XV, ol/opx is 3/2 (Table 1). A late-stage Fe-Ti-rich component was created by combining ilmenite, clinopyroxene (augite), and plagioclase as had been done for CMV, VI, and V_II. The proportions of harzburgite mantle in urKREEP-free mixes (CMX, X_II, XI, and XV) are elevated (0.8–0.85 opposed to 0.5–0.6, Figure 1). FeO and TiO_2 in CMX, X_II, XI, and XV are more variable. CaO and Al_2O_3 contents of the starting compositions CMX, X_II, XI, and XV are reduced due to the missing urKREEP component in the mixture.

We further exclude the urKREEP component for two reasons: First, its major element composition is poorly constrained (Singletary & Grove, 2008). Second, urKREEP is often considered a trace element signature, rather than a major cumulate composition, and it is unclear if urKREEP was directly involved in remelting during the IBC overturn (Laneuville et al., 2013).

2.2. Synthesis of Starting Materials

Starting materials were synthesized by mixing high-purity oxides and carbonates (SiO_2, Al_2O_3, TiO_2, MgO, Cr_2O_3, $CaCO_3$, $MnCO_3$, K_2CO_3, Na_2CO_3). MgO was pre-heated at 1,000°C to remove hydroxide or carbonate. The powders were homogenized under ethanol in an agate mortar, subsequently dried and decarbonated at 1,000°C for

Journal of Geophysical Research: Planets

10.1029/2023JE008239

Table 1
Starting Material Compositions

Mineralogical and chemical composition of starting materials							
	CMV	CMVI	CMVI_II	CMX	CMX_II	CMXI	CMXV
Early cumulate (Harzburgite)	0.5* (0.5ol + 0.5opx)	0.5*(0.5ol + 0.5opx)	0.6*(0.5ol + 0.5opx)	0.8*(0.55ol + 0.45opx)	0.85* (0.55ol + 0.45opx)	0.8* (0.6ol + 0.4opx)	0.82*(0.6ol + 0.4opx)
IBC	0.2* (0.2cpx + 0.8ilm)	0.1* (0.7cpx + 0.1ilm + 0.2pl)	0.09* (0.7cpx + 0.1ilm + 0.2pl)	0.2* (0.44cpx + 0.44ilm + 0.12pl)	0.15* (0.5cpx + 0.5ilm)	0.2* (0.52cpx + 0.45ilm + 0.03pl)	0.18* (0.33cpx + 0.67ilm)
urKREEP	0.3	0.4	0.31				
urKREEP-containing				No urKREEP			
	CMV	CMVI	CMVI_II	CMX	CMX_II	CMXI	CMXV
SiO_2	37.48	43.58	43.2	40.78	41.79	40.59	39.64
TiO_2	8.18	1.28	1.43	4.86	4.42	5.26	9.53
Al_2O_3	5.14	7.03	6.8	3.11	1.69	2.82	2.78
FeO	16.16	12.89	13.1	17.58	17.84	17.48	15
CaO	3.72	5.07	5.4	2.51	1.87	2.51	3.9
MnO	0.07	0.03		0.1	0.11	0.09	0.15
MgO	26.58	28.2	28.57	29.97	31.67	29.96	27
Na_2O	0.26	0.4	0.51	0.05	0.05	0.06	0.16
K_2O	0.25	0.34	0.05	0.08	0.02	0.09	0.05
Cr_2O_3	0.16	0.16					
Mg#	0.74	0.8	0.8	0.75	0.76	0.75	0.76

Note. The top part of the table lists the different cumulate components in our hybrid mantle starting material compositions, that is, harzburgite, IBC, and urKREEP. For harzburgite and IBC, modal mineralogy is given. Harzburgite bulk composition for CMV, VI, and VI_II taken from Hess and Parmentier (1995), urKREEP from Warren and Wasson (1979). Mineral abbreviations: ilmenite = ilm, plagioclase = pl, orthopyroxene = opx, clinopyroxene = cpx, olivine = ol. As an example, starting material CMV contains 50 wt% harzburgite (consisting of a 50/50 mix of olivine and orthopyroxene), 20 wt% IBC (consisting of a mix of 80 wt% ilm and 20 wt% cpx), and 30 wt% of urKREEP (Warren & Wasson, 1979). The lower part of the table displays the chemical composition of the starting materials. Note that the starting materials labeled as CMX_ do not contain an urKREEP component.

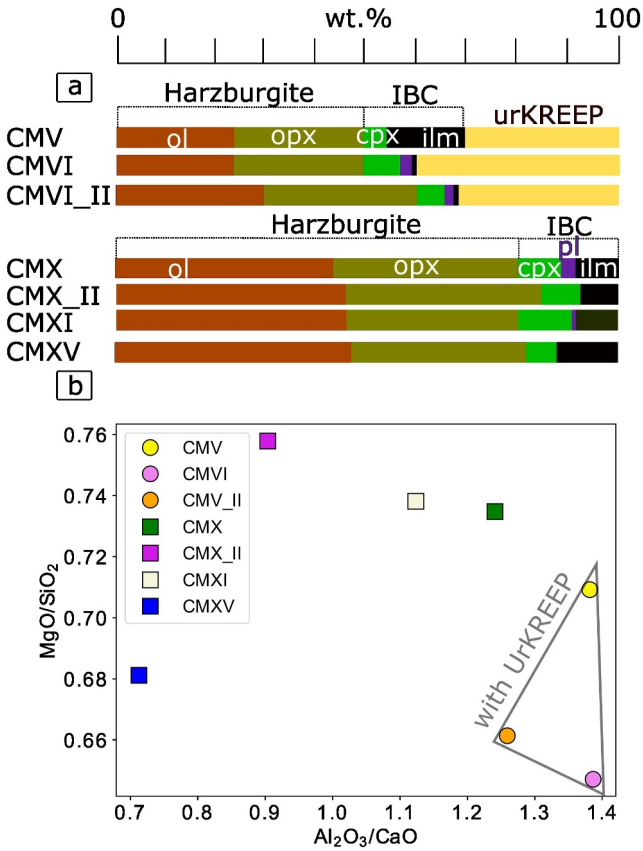

Figure 1. (a) Modal mineralogy and composition of the starting materials CMV, VI, and VI_II with fixed harzburgite (olivine + orthopyroxene: 0.5ol + 0.5opx), IBC, and urKREEP components. The IBC component contains variable amounts of ilmenite (ilm), clinopyroxene (cpx), and plagioclase (pl). CM X–XV do not contain an urKREEP component but variable amounts of ol, opx, cpx, ilm (+pl). (b) The starting material compositions, simulating a hybrid lunar mantle, depicted in Al_2O_3/CaO versus MgO/SiO_2 space (wt% ratios). Compositions with urKREEP and pl have higher Al_2O_3/CaO compared to the other starting compositions. Consequently, CMXV has low MgO/SiO_2 with high ilm/cpx and ol/opx. CM_VI and VI_II contain high abundances of urKREEP, pl, and cpx and these compositions are characterized by lower MgO/SiO_2. Color scheme for (a): brown = ol, olive green = opx, bright green = cpx, black = ilm, violet = pl, sand yellow = urKREEP.

at least 10 hr, followed by additional grinding and homogenization in a mortar. Iron was added to the decarbonated mixture as hematite (Fe_2O_3). The Fe-bearing, homogeneous mixtures were vitrified at 1,400°C for 30 min, crushed and ground to a powder and stored dry in a desiccator.

2.3. Experimental Methods

High-pressure experiments were conducted in an end-loaded piston-cylinder apparatus (Boyd & England, 1960). Starting material mixtures were loaded into lidded graphite containers, which were inserted into a Pt outer capsule (Figure 2a) and welded shut after having spent a minimum of 24 hr in a drying furnace at 110°C. The capsules were placed into ½ inch piston-cylinder assemblies consisting of two inner cylinders made of 6 mm O.D. crushable alumina (TKF Frömgen GmbH). The inner parts of the assembly are surrounded by a graphite furnace, an outer Duran glass cylinder (Schott GmbH) and a talk sleeve. Calibration of the assembly has been performed using the quartz-coesite transition (Bose & Ganguly, 1995) and the $MgCr_2O_4 + SiO_2 = MgSiO_3 + Cr_2O_3$ reaction (Klemme & O'Neill, 1997), which results in a friction correction of −13%. Based on our pressure calibration, quoted pressures are accurate within 0.07 GPa. We used a hot piston-in technique. Run temperatures during the experiment were monitored and controlled using a W-Re-thermocouple (Type D) in conjunction with a Eurotherm controller (Schneider Electric, Germany). Experiments were quenched by shutting off the electric power. The quench rates are faster than 120 K/s for the first ~300°C. All experimental run conditions, together with a list of all phases present after the run, can be found in Table 2. Most experiments were conducted at either 1,300°C ($n = 5$) or 1,400°C ($n = 7$).

2.4. Electron Microprobe Analyses of Minerals and Quenched Melts

The run products (Figure 2) were analyzed using a JEOL JXA 8530 F Hyperprobe at the Institut für Mineralogie at the Universität Münster (Germany) in wavelength-dispersive mode (WDS) (details are given in Haupt, Renggli, Rohrbach, Berndt, & Klemme, 2024). EPMA measurements of the quenched silicate melts were performed using an acceleration voltage of 15 kV and a beam current of 10 nA. The beam current for silicate and oxide minerals was set to 15 nA. Silicate and oxide minerals were analyzed with a beam diameter of 1–5 µm and quenched melts were analyzed with a defocused beam (diameter between 10 and 20 µm). The matrix corrections were made according to the $\varphi(\rho z)$ procedure (Armstrong, 1991). Even though the runs were quenched fast, some quench crystallization of olivine was inevitable in runs with MgO and TiO_2-rich melts (Figure 2c). Therefore, glasses in these runs were analyzed randomly (n = 10–50; Haupt, Renggli, Rohrbach, Berndt, & Klemme, 2024) to get more representative data with better statistics. Nevertheless, it is obvious from the error bars of MgO in Figure 4 that the uncertainties of the MgO analyses are higher in these runs than in experiments without quench crystallization.

2.5. Constraints on Oxygen Fugacity (fO_2)

The graphite-lined platinum capsules impose an fO_2 maximum of ΔIW + 2 at our run temperatures (ΔIW ± x denotes the value of fO_2 relative to the iron-wüstite buffer in log10 units at given T; Holloway et al., 1992; Krawczynski & Grove, 2012; Medard et al., 2008). Our spinel and orthopyroxene measurements indicate virtually no Fe^{3+} in these minerals, which is taken as evidence for an fO_2 about IW. Additionally, we could not detect any iron metal in our runs, which would have indicated an fO_2 corresponding to <ΔIW–2 (Krawczynski & Grove, 2012). In summary, these observations bracket the fO_2 of our experiments near the conditions predicted for the lunar basalt source (~ΔIW–0.5; Nicholis & Rutherford, 2009; Sato et al., 1973; Weitz et al., 1997).

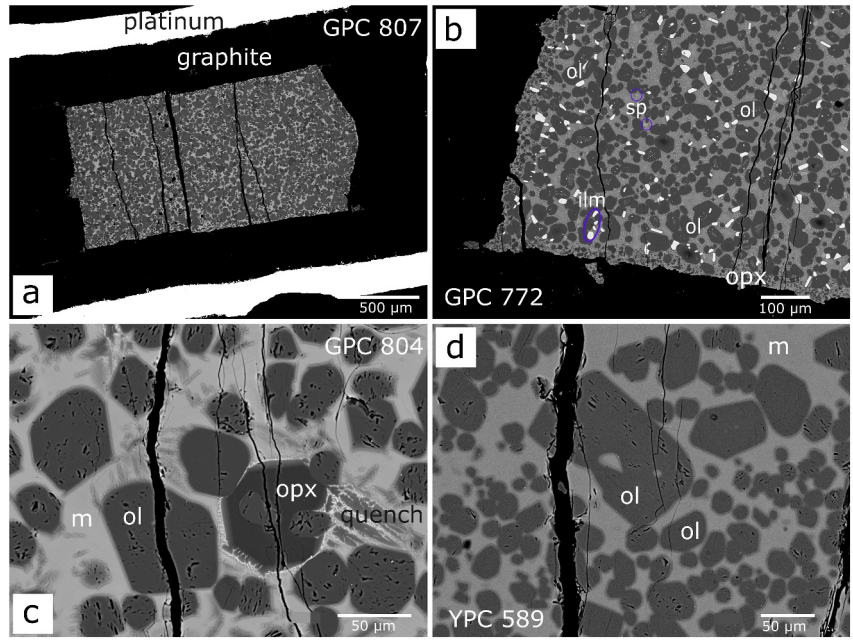

Figure 2. Back-scattered electron images (BSE) of piston-cylinder experiments in graphite-lined platinum capsules. (a) Overview image of experimental run at 1.5 GPa and 1,300°C, cumulate (CM) XI with olivine, orthopyroxene, and melt ($F = 0.3$). (b) CMV at 1.5 GPa and 1,230°C with olivine (ol), orthopyroxene (opx), traces of ilmenite (ilm, bright white BSE contrast) and spinel (sp, gray accessories), and melt (m). ilm and sp circled in blue. (c) CMX at 1.5 GPa and 1,400°C with olivine, traces of orthopyroxene and melt. Note that quench textures in the melt were avoided during analysis. (d) CMVI_II at 1.5 GPa and 1,350°C with olivine and melt ($F = 0.55$).

2.6. Attainment of Equilibrium

Equilibrium between minerals and melts is indicated by low standard deviations of multiple analyzes of mineral phases and quenched melts only runs with visible quench mineralization had higher uncertainties (see discussion above, e.g., runs GPC 772, GPC 807). Run durations were chosen according to experiments conducted under similar conditions (Delano, 1980; Singletary & Grove, 2008). Furthermore, we calculated Fe-Mg mineral-liquid exchange coefficients ($K_D^{Fe–Mg}$) to assess whether experimental run durations were sufficient to attain equilibrium (Haupt, Renggli, Rohrbach, Berndt, & Klemme, 2024). The K_D vary with pressure, temperature, and also TiO_2 of the melt and are in good agreement with experiments conducted under similar conditions and compositions (Krawczynski & Grove, 2012; Singletary & Grove, 2008; Wagner & Grove, 1997; Xirouchakis et al., 2001).

Moreover, linear least squares regression analysis of the measured phase compositions was used to determine Fe loss, phase proportions, and degree of melting (F). We found that a maximum of 2 wt% Fe was lost to the capsule. Mass balance, which was attained using linear least squares regression, mostly yields small residuum (r^2) values (<1). These observations together with homogeneous and unzoned crystals in the runs demonstrate that equilibrium was attained during the experimental runs.

3. Experimental Results

3.1. Melt Compositions Derived From Melting of a Hybrid Lunar Mantle Compared to Lunar Volcanic Glass Compositions

All experiments contain glass (Table 2, Figure 2; degree of partial melting (F_{melt}) = 0.18–0.75) in equilibrium with olivine ($F_{olivine}$ = 0.22–0.58) and some experiments contain orthopyroxene ($F_{opx} < 0.3$), summarized in Tables 2 and 3. The experiments that contained both olivine and orthopyroxene (Figures 2a and 2c) were run at lower temperatures (<1,400°C for all CM starting materials, except CMX, where traces of orthopyroxene are present at 1,400°C) showing low degrees of partial melting ($F_{melt} < 0.5$; Table 2; Haupt, Renggli, Rohrbach, Berndt, & Klemme, 2024). Olivine in the experiments is forsteritic ($olivine_{Fo}$ = 79–91 mol%), and the fayalite component increases with decreasing temperature (e.g., CMXV $ol_{1400–1300°C}$: $Fo_{90–84}Fa_{10–16}$). Orthopyroxene

Table 2
Experimental Run Conditions (P in GPa, T in °C, Duration t in h) Together With Information on the Starting Material (CMV–XV, Table 1), Phases Present, and Phase Proportions, Calculated Using Linear Least Squares Regression Given in Brackets (1–100 wt%)

Run ID	Starting Material	P [GPa]	T [°C]	t[h]	Phases and proportions	Fe loss [wt%]	r^2	Calculated melt densities [g/cm³]	Olivine $K_D^{Fe\text{-}Mg}$
YPC_587	XV	1.5	1,400	6	ol(25), melt(73)	2	0.3	3.27	0.29
YPC_588	X_II	1.5	1,400	2	ol(38.5), melt(61.5)		0.9	3.18	0.29
YPC_589	VI_II	1.5	1,350	8	ol(43), melt(55)	2	0.7	3.06	0.27
GPC_868	X_II	1.5	1,300	8	ol(51), opx(30), melt(18)		0.2	3.52	0.13
GPC_869	XV	1.5	1,300	8	ol(41), opx(15), melt(43)		0.7	3.38	0.19
GPC_870	VI_II	1.5	1,250	10	ol(47), opx(13), melt(40)		0.2	3.07	0.26
GPC_847	XI	1.5	1,350	8	ol(58), opx(6), melt(35)	1	0.5	3.32	0.14
GPC_804	X	1.5	1,400	5	ol(48), melt(51), opx(tr)	1	0.7	3.21	0.27
GPC_805	X	1.5	1,300	15	ol(56), opx(15), melt(29)		0.3	3.45	0.14
GPC_806	XI	1.5	1,400	5	ol(50), melt(49)	1	0.5	3.25	0.26
GPC_807	XI	1.5	1,300	15	ol(56), opx(14), melt(30)		0.4	3.36	0.16
GPC_772	V	1.5	1,250	5.5	ol(46), opx(13), melt(38), sp(tr), ilm(3)		0.4	3.38	0.21
GPC_769	V	1.5	1,400	5	ol(42), melt(58)		0.5	3.32	0.21
GPC_770	V	1.5	1,500	2.5	ol(21.7), melt(75)	3.3	0.2	3.19	0.26
GPC_775	V	2.5	1,500	3.5	ol(36), melt(63)	1	0.7	3.46	0.19
GPC_784	V	2.5	1,400	5.3	ol(43), melt(56)	1	0.3	3.56	0.20
GPC_785	V	0.8	1,320	16	ol(44), melt(55), sp(tr)	1	0.8	3.20	0.22
GPC_777	VI	1.5	1,400	5.25	ol(33), melt(65)	2	0.1	3.09	0.31
GPC_782	VI	1.5	1,300	6	ol(42), opx(16), melt(41)		0.2	3.09	0.29

Note. Fe-loss in wt% was calculated using mass balance constraints. The r^2 values (residuum) are small (<1), indicating good agreement of starting material composition and analyzed phases (least squares including major components except K_2O, Cr_2O_3, MnO, Na_2O, and NiO). Olivine = ol, orthopyroxene = opx, ilmenite = ilm, spinel = sp. Melt densities as a function of composition, pressure, and temperature were calculated using the model of Bottinga and Weill (1970). More details can be found in Haupt, Renggli, Rohrbach, Berndt, and Klemme (2024).

compositions are enstatite-rich ($Wo_{0–3}En_{80–85}Fs_{13–18}$). Traces of spinel are present in two runs of CMV at lower pressures (0.8 GPa: ID GPC_785) and low temperature (1,250°C: ID GPC_772). The experiment with CMV at 1,250 C contains traces of ilmenite (Tables 2 and 3, Figure 2b and Haupt, Renggli, Rohrbach, Berndt, & Klemme, 2024).

Mg# (molar ratio of Mg/(Mg + Fe)) of the experimentally produced glasses cover the range defined by the lunar pyroclastic glasses (Figure 3). Mg# of melts produced by melting the CMVI and VI_II starting materials, and the runs with CMV at high degrees of melting ($F_{melt} \geq 0.65$), yield Mg# between 0.68 and 0.75, which are even higher than the Mg# of lunar high-Ti pyroclastic glasses (Mg# = 0.45–0.68, Figure 3). Mg# of melts from CMV with lower degrees of melting ($F_{melt} \leq 0.65$) plot within the range of the red and black high-Ti lunar picritic glasses (Figures 3 and 4). In quenched melts derived from starting materials CMX, XI, XI_II, and XV, glass Mg# and SiO_2 contents are much lower, which can be explained by the presence of orthopyroxene in the runs as a consequence of lower run temperatures and lower degrees of melting (Figure 3) and hence it is orthopyroxene that exerts a strong control on the Mg# of the melt (CMXI, Figure 3). Glass compositions in experiments on starting materials CMX, X_II, and XI are within the range of the FeO of the volcanic glasses (17.5–22.5 wt%). The MgO of all experimental glasses cover the entire array of MgO contents of the lunar picritic glasses (i.e., 10–19 wt% MgO). Especially, the glasses of CMV match the relatively high MgO of high-Ti pyroclastic glasses (10–15 wt% MgO).

The closest match between experimental quenched melts and natural pyroclastic yellow to red-black lunar picritic glass compositions is shown in the SiO_2-TiO_2 space, mainly reproduced by the experimental quenched melt compositions of all four urKREEP-free starting materials (Figure 4a: CMX, X_II, XI, XV). Melts with high TiO_2 contents were found predominantly at lower run temperatures of ~1,300°C and consequently lower

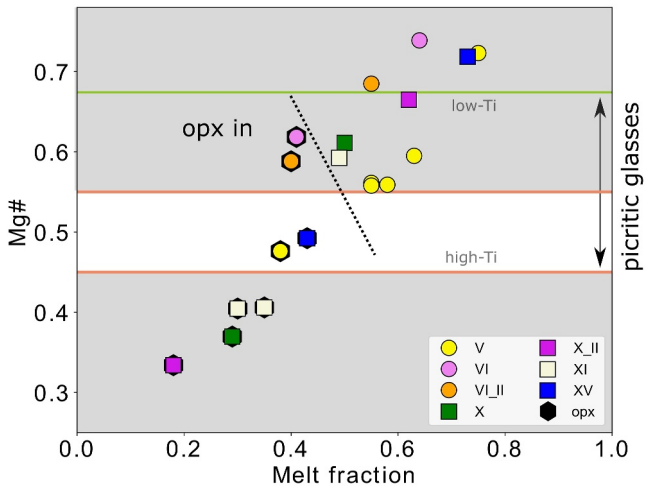

Figure 3. Mg# of the experimentally produced quenched melts of a hybrid lunar cumulate mantle as a function of melt fraction. The black dotted line represents the orthopyroxene-in line with opx present at lower melt fractions. The white band that is limited by orange horizontal lines marks the range of lunar picritic glasses of high-Ti pyroclastic glasses, and the green line marks the highest Mg# of green/VLT pyroclastic glasses (Delano, 1986; Shearer & Papike, 1993).

degrees of melting (F_{melt} = 0.18–0.38: Table 2, Figures 2–4). The quenched melts of urKREEP-bearing starting materials (Figure 1 CMV, VI, and VI_II) cover the extremes of red-black picritic glasses (CMV) on the one hand and low-Ti basalts on the other hand (CMVI, VI_II) (Figures 2–5) and are in fact the only ones clearly overlapping with lunar samples. The partial melts of both the CMVI and CMVI_II starting materials have SiO_2 contents (45–47 wt%), which is higher compared to other experimental glasses (Figure 4a).

The CaO and TiO_2 contents of the experimental quenched melts are close to those of the lunar orange and black pyroclastic glasses (Figure 4b). The experimental glasses cover the lunar pyroclastic glasses in CaO (6–8 wt%) but show greater variability (4.5–10 wt%). CaO and TiO_2 contents in the melts are high when the degree of melting is low and both ol + opx are residual phases. In the CaO-TiO_2 space, the trend of experimental glasses is similar to the trend identified by the experimental glasses of Singletary and Grove (2008), but generally shows higher TiO_2. Melts of starting material CMV and CMXI constrain the best matches in CaO and TiO_2. Quenched melts from experiments on CMVI (1,300°C) and VI_II melts not only have elevated CaO and low TiO_2, which resemble high-Al basalts, but also match these basalts in the MgO/SiO_2-TiO_2/CaO space. TiO_2/CaO in glasses of experiments with starting material CMV, X, and XI yield TiO_2/CaO close to the lunar pyroclastic glasses (1–2.5, Figure 4c), whereas their MgO/SiO_2 is matched mainly by the 1,400°C experiments (MgO/SiO_2 = 0.3–0.45,

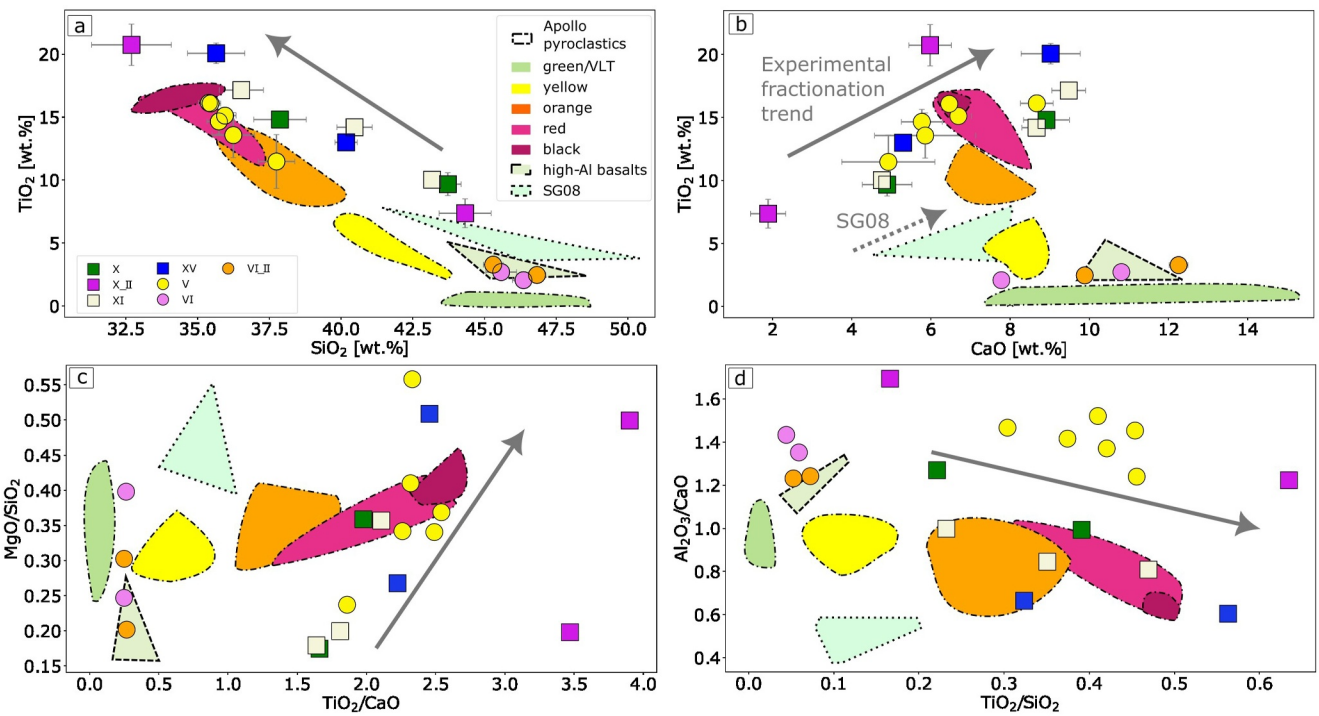

Figure 4. Chemical composition of the Apollo 14 high-Al basalts and picritic glass beads outlined as colored areas (i.e., bordered with point-dashed; data sources: Delano, 1986; Papike et al., 1997; Shearer & Papike, 1993) compared to our experimental quenched melts (circles: KREEP-bearing and squares: KREEP-free starting materials). The light green area bordered by dashes depicts the compositions of low-Ti and high-Al mare basalts (Fagan et al., 2014; Hallis et al., 2004). The compositions of experimental quenched melts of Singletary and Grove (2008), denoted as SG08, are depicted in the turquoise triangle and surrounded by a dotted line. (a) SiO_2 versus TiO_2 (b) CaO versus TiO_2 (c) TiO_2/CaO versus MgO/SiO_2, and (d) TiO_2/SiO_2 versus Al_2O_3/CaO. See Haupt, Renggli, Rohrbach, Berndt, and Klemme (2024) for Mg# versus TiO_2 and SiO_2 versus FeO.

Table 3
Experimental Results and EPMA Analyses of Minerals (olivine = ol, orthopyroxene = opx, ilmenite = ilm, spinel = sp) and Quenched Melt (gl), Given in Oxides in wt

Run ID	Phase	St mat	P	T	F	n	SiO_2	TiO_2	Al_2O_3	Cr_2O_3	FeO	MgO	CaO	Na_2O	K_2O	MnO	Total
GPC 847	gl	XI	1.5	1,350	0.35	8	40.5(6)	14.2(6)	7.3(4)	0.40(5)	18.9(5)	7.3(3)	8.7(4)	0.24(3)	0.39(6)	0.23(1)	98.1
	opx					5	55.7(1)	0.83(7)	1.21(6)	0.57(1)	10.2(1)	31.4(1)	0.75(2)	<DL	<DL	0.11(1)	100.7
	ol					5	39.68(9)	0.19(6)	0.07(2)	0.22(2)	16.3(1)	43.8(1)	0.12(1)	<DL	<DL	0.11(2)	100.5
GPC 772	gl	V	1.5	1,250	0.38	10	35.5(4)	16.5(5)	10.9(1)	0.23(2)	16.5(2)	8.4(2)	8.7(4)	0.76(6)	0.65(6)	<DL	98.1
	ilm						0.11(4)	54.9(3)	1.59(2)	2.68(2)	27.6(1)	11.6(1)	0.19(4)	<DL	<DL	0.11(2)	98.7
	sp					4	1.3(6)	6.2(6)	36(2)	19.2(9)	19.9(4)	15.2(3)	0.3(1)	<DL	<DL	0.09(1)	98.6
	ol					3	39.4(1)	0.24(9)	0.08(1)	0.08(1)	17.4(1)	43.00(7)	0.17(4)	<DL	<DL	0.07(1)	100.5
	opx					4	51.7(3)	1.5(2)	6.1(5)	0.77(2)	10.9(4)	28.3(3)	1.22(8)	<DL	0	0.07(1)	100.6
GPC 806	gl	XI	1.5	1,400	0.49	6	43.2(3)	10.0(3)	4.7(1)	0.54(5)	18.9(3)	15(1)	4.8(2)	0.25(3)	0.22(1)	0.21(1)	98.2
	ol					5	40.1(1)	0.23(1)	0.06(3)	0.24(1)	14.7(1)	45.3(2)	0.12(2)	<DL	<DL	0.11(1)	100.9
GPC 807	gl	XI	1.5	1,300	0.3	6	36.5(8)	17.1(4)	7.7(2)	0.33(6)	19.1(4)	7.3(2)	9.5(4)	0.27(5)	0.44(6)	<DL	98.3
	ol					4	39.45(8)	0.17(3)	0.06(1)	0.20(2)	18.2(2)	42.2(1)	0.15(3)	<DL	<DL	0.13(3)	100.5
	opx					3	54.7(4)	1.14(3)	1.9(2)	0.72(7)	11.2(1)	30.22(4)	0.98(1)	<DL	<DL	0.09(1)	101.0
GPC 784	gl	V	2.5	1,400	0.55	26	36.0(4)	15.1(5)	9.2(5)	0.59(6)	17.1(4)	12.3(1)	6.7(3)	0.61(7)	0.50(7)	<DL	98.1
	ol					10	40.0(3)	0.21(4)	0.125(1)	0.19(2)	13.2(3)	46.7(3)	0.12(1)	0.011(6)	<DL	0.07(1)	100.7
GPC 785	gl	V	0.8	1,320	0.55	30	35.4(4)	16.1(6)	9.4(4)	0.48(6)	17.1(4)	12.1(6)	6.5(3)	0.61(6)	0.50(5)	<DL	98.1
	ol					10	40.1(2)	0.25(4)	0.11(2)	0.22(2)	14.1(3)	46.0(2)	0.13(1)	<DL	<DL	0.07(1)	100.9
	sp					10	0.19(3)	9.8(2)	20.3(1)	32.2(2)	20.3(6)	15.7(2)	0.09(1)	<DL	<DL	0.14(1)	98.6
GPC 769	gl	V	1.5	1,400	0.53	36	35.7(4)	14.7(1)	8.8(7)	0.54(7)	18.5(4)	13(2)	5.8(5)	0.55(8)	0.44(6)	<DL	98.2
	ol					20	39.7(1)	<DL	0.13(1)	0.20(2)	13.4(1)	46.2(2)	0.15(1)	<DL	<DL	<DL	99.8
GPC 770	gl	V	1.5	1,500		25	37.7(6)	11(2)	7(2)	0.48(8)	14.4(6)	21(6)	5(1)	0.49(8)	0.39(8)	<DL	98.2
	ol					5	40.9(2)	0.19(7)	0.13(2)	<DL	8.9(3)	50.4(2)	0.14(3)	0.02(1)	<DL	<DL	101.0
YPC 587	gl	XV	1.5	1,400	0.73	8	40.2(4)	13.0(4)	3.52(8)	0.75(8)	14.3(3)	20.44(6)	5.3(1)	0.31(1)	<DL	0.28(1)	98.0
	ol					5	40.8(2)	<DL	<DL	0.24(3)	10.1(2)	49.22(1)	<DL	<DL	<DL	<DL	100.4
YPC 588	gl	X_II	1.5	1,400	0.62	15	44.3(9)	7(1)	3.2(5)	0.43(7)	20(1)	22(5)	1.9(4)	0.33(3)	<DL	<DL	99.5
	ol					5	40.3(2)	<DL	<DL	<DL	12.4(2)	47.7(2)	<DL	<DL	<DL	<DL	100.4
YPC 589	gl	VI_II	1.5	1,350	0.55	11	46.8(3)	2.47(9)	12.2(3)	<DL	11.6(3)	14(1)	9.9(2)	0.75(7)	0.27(4)	<DL	98.1
	ol					5	40.4(2)	<DL	0.14(9)	<DL	10.9(2)	48.7(2)	0.24(5)	<DL	<DL	<DL	100.4
GPC 868	gl	X_II	1.5	1,300	0.18	21	33(1)	21(2)	7.3(4)	0.38(9)	23.0(7)	6.5(8)	6.0(5)	1.1(1)	0.39(4)	<DL	98.1
	ol					5	39.00(6)	<DL	<DL	<DL	19.6(3)	41.6(1)	<DL	<DL	<DL	<DL	100.1
	opx					5	54.4(3)	1.15(7)	1.7(1)	0.69(6)	12.0(2)	29.9(2)	<DL	<DL	<DL	<DL	100.4
GPC 869	gl	XV	1.5	1,300	0.43	22	35.6(1)	20.1(8)	5.5(3)	0.65(9)	17.5(3)	9.5(9)	9.0(7)	0.44(6)	0.23(2)	<DL	98.6
	ol					5	39.7(1)	<DL	<DL	0.25(3)	15.4(2)	44.5(2)	<DL	<DL	<DL	<DL	99.8
	opx					5	55.1(3)	1.36(5)	1.33(7)	0.86(5)	9.74(8)	31.0(2)	1.05(2)	<DL	<DL	<DL	100.5
GPC 870	gl	VI_II	1.5	1,250	0.4	12	45.3(3)	3.3(3)	15.2(3)	<DL	11.4(3)	9.1(7)	12.3(2)	1.07(6)	0.36(3)	<DL	98.0
	ol					5	39.6(2)	<DL	0.17(4)	<DL	14.8(4)	45.2(4)	0.28(6)	<DL	<DL	<DL	100.0
	opx					5	53.5(1)	0.1(2)	5(1)	0.6(1)	9.2(2)	29.2(6)	2.23(9)	<DL	<DL	<DL	100.2
GPC 804	gl	X	1.5	1,400	0.5	10	43.7(5)	9.7(9)	6.2(7)		17.8(6)	16(4)	4.9(6)	<DL	0.24(4)	<DL	98.2
	ol					4	40.1(3)	<DL	<DL	<DL	13.9(1)	46.3(2)	<DL	<DL	<DL	<DL	100.4
	opx					3	56.9(4)	0.70(3)	0.84(3)	<DL	8.60(4)	33.2(1)	0.50(2)	<DL	<DL	<DL	100.8
GPC 805	gl	X	1.5	1,300	0.29	12	37.9(9)	14.8(6)	8.9(3)	<DL	20.1(7)	6.6(4)	8.9(6)	0.48(4)	0.42(6)	<DL	98.1
	ol					5	39.0(4)	<DL	<DL	<DL	18.2(2)	42.3(3)	0.1(1)	<DL	<DL	<DL	99.7
	opx					5	54.8(2)	1.1(2)	1.9(1)	<DL	11.6(1)	30.3(3)	0.84(6)	<DL	<DL	<DL	100.8
GPC 775	gl	V	2.5	1,500	0.63	20	36.2(7)	14(2)	8(1)	0.57(6)	18.0(4)	15(5)	6(1)	0.57(1)	0.44(7)	<DL	98.4

Table 3
Continued

Run ID	Phase	St mat	P	T	F	n	SiO_2	TiO_2	Al_2O_3	Cr_2O_3	FeO	MgO	CaO	Na_2O	K_2O	MnO	Total
	ol					5	40.6(2)	0.21(4)	0.16(5)	0.18(2)	11.1(2)	48.6(2)	0.14(2)	0.02(1)	<DL	0.09(1)	101.2
GPC 777	gl	VI	1.5	1,400	0.64	10	46.4(4)	2.1(4)	11.1(6)	<DL	11.6(2)	18.5(7)	7.8(2)	0.64(7)	<DL	<DL	98.0
	ol					5	40.7(1)	<DL	0.14(5)	<DL	9.72(7)	49.7(1)	0.19(2)	<DL	<DL	<DL	100.4
GPC 782	gl	VI	1.5	1,300	0.41	10	45.6(4)	2.7(2)	14.6(3)	<DL	12.4(4)	11.3(6)	10.8(3)	0.78(8)	<DL	<DL	98.1
	ol					5	39.75(7)	<DL	0.12(2)	<DL	14.6(2)	45.4(1)	0.28(5)	0.02(1)	<DL	<DL	100.3
	opx					5	53.5(5)	0.38(8)	5.0(6)	0.43(4)	8.9(3)	30.1(3)	1.63(6)	<DL	<DL	<DL	100.0

Note. % with absolute errors on the last digits (σ) given in brackets. F = phase proportions ($0 < F < 1$) calculated by linear least squares method and n = number of analyzes; <DL below detection limit. P = pressure in GPa, T = temperature in °C, st mat = starting material, run ID = experimental run number.

Figure 4d). The MgO/TiO_2 of most quenched melts does not compare with the natural samples, which have all very similar MgO/SiO_2. The MgO/SiO_2 requires a means to be buffered.

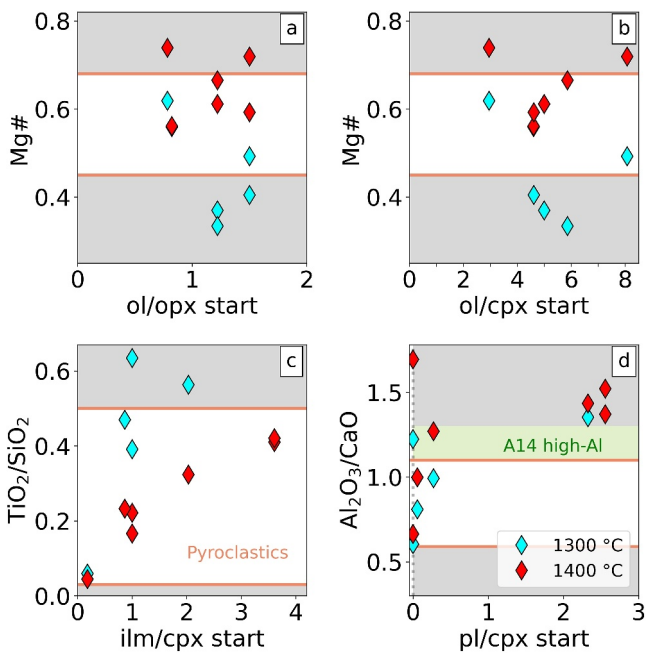

Figure 5. Experimental glass compositions on the ordinate plotted against the mineralogical composition of the starting materials on the abscissa (e.g., ol/opx start). The composition of the experimental quenched melts was color coded for run temperature (turquoise = 1,300°C or red = 1,400°C, comp. Table 2) (a) ol/opx versus Mg#, (b) ol/cpx versus Mg# (c) ilm/cpx versus TiO_2/SiO_2 (d) pl/cpx versus Al_2O_3/CaO. Orange lines delineate the range of the Apollo picritic glasses (Delano, 1986; Papike et al., 1997; Shearer & Papike, 1993). The green band in (d) depicts the range of Apollo14 high-Al mare basalts (Fagan et al., 2014, and compilation of Wieczorek et al., 2006) (a + b) the degree of melting influences Mg#, with the 1,400°C runs having the higher Mg# (a) sorted by T, higher Mg# of glasses correlate with ol/opx. (b) high Mg# correlate with high ol/cpx and 1,400°C, but are inversely correlated with the glasses in the 1,300°C runs. (c) The ilm/cpx of the starting material correlates with TiO_2/SiO_2 of the experimental quenched melt, high ilm/cpx in the starting material yields high-Ti quenched melts. (d) high Al_2O_3/CaO is found in runs with an urKREEP component in the starting material and in starting material CMX_II with no pl in the starting material (Figures 1 and 4d). Abbreviations: ilm = ilmenite, pl = plagioclase, cpx = clinopyroxene, ol = olivine.

Quenched melts of CMV, CMVI, and CMVI_II have high Al_2O_3/CaO of 1.2–1.5 compared to glasses from urKREEP-free starting materials and natural lunar pyroclastic glasses (Figure 4d). Starting material CMVI yields glasses with Al_2O_3/CaO higher than quenched melts from CMVI_II (1.4 instead of 1.2: Figure 4d). Al_2O_3/CaO of glasses from CMXI and XV are comparatively low (Figure 4d: Al_2O_3/CaO = 0.7–1 and ~0.6, respectively), covering a wide range of the high-Ti to intermediate-Ti picritic glasses (0.3–0.6). Quenched glasses of experiments on CM V and XV are higher than the natural sample suite.

4. Discussion

4.1. Effects of Hybrid Mantle Mineralogy

4.1.1. Pyroxene

A major component of each starting material (CM) is a harzburgite (50%–80%, Table 1, Figure 1), which causes high Mg# of the bulk compositions (Mg# = 0.74–0.8; Table 1). Mg# of the partial melts, however, vary and are strongly controlled by the appearance of orthopyroxene; for example, crystallization of 6–12 wt% of orthopyroxene results in a drop in melt Mg# of 0.2–0.3 units compared to experiments without orthopyroxene (Figure 3). In runs with high degrees of partial melting, orthopyroxene is not stable ($F_{melt} > 0.4$: Figure 3). Its proportion in the harzburgite component of the starting material influences the extent to which the Mg# of the experimental glasses matches lunar glasses: CMXI and XV both contain more olivine than orthopyroxene in the harzburgite cumulate component (ol/opx = 3/2) and quenched melts in runs with these starting compositions do match the range of lunar pyroclastic glasses (Figures 1 and 5, Tables 2 and 3).

4.1.2. Composition of the IBC Layer

The TiO_2 content of the quenched melt is strongly controlled by ilmenite and clinopyroxene in the IBC component of the starting material. High TiO_2 in the melt is achieved by melting a starting material cumulate with ilm/cpx proportions of 1/1 (CMX, X_II, XI), 2/1 (CMXV), and 4/1 (CMV) (Figures 4a and 5c). The correlation of TiO_2/SiO_2 of the experimental quenched melts with ilm/cpx in the starting material is nearly linear for both 1,300 and 1,400°C runs and almost all experimental glass compositions overlap with the range of lunar pyroclastic glasses (Figure 5c). The lower the ilmenite

proportion in the starting material cumulate, the lower the melt fraction needs to produce high-TiO_2 quenched melts. Experimental glasses of starting materials with ilm/cpx = 1/1 (CM X, X_II; Table 1) produce high-TiO_2 glasses with F_{melt} = 0.29 and 0.18, respectively, at 1,300°C, whereas CMV with ilm/cpx = 4/1 in experiments successfully reproduce high-Ti lunar pyroclastic glass compositions at F_{melt} = 0.38 (Figures 1 and 5, Tables 1 and 2). The lowest ratio of ilm/cpx (1:10) in our starting material cumulate yields low-Ti quenched melts (2–5 wt% TiO_2), similar to the A14 high-Al mare basalts (Figures 4a and 4d). The best match of experimental glasses (in terms of TiO_2/SiO_2, Al_2O_3/CaO, and TiO_2/SiO_2) with lunar pyroclastic glasses was achieved by starting material cumulate CMXI with ilm/cpx = 1/1, ol/opx = 3/2 and ol/cpx = 4.6 (Figure 5).

Starting materials to which plagioclase was added as part of the IBC component have elevated Al_2O_3/CaO compared to starting materials without plagioclase (Figure 1, all except X_II and XV). Partial melting of these starting materials results in quenched melts with Al_2O_3/CaO similar to those of the high-Ti pyroclastic glasses (Figures 4d and 5d), indicating that plagioclase in the lunar cumulate source is required and that the efficiency of plagioclase flotation during LMO crystallization was less than 100% (Charlier et al., 2018). Starting materials CMX and XI contain 2–6 wt% plagioclase (ilm/cpx/pl in IBC = 1/1/0.25 and 1/1/0.1, respectively) and their glasses cover the Al_2O_3/CaO range of pyroclastic glasses (0.6–1.1, Figure 5d). Quenched melts in experiments using starting materials CMX_II and XV, which lack plagioclase in the bulk (Figure 1), show variable Al_2O_3/CaO due to different amounts of clinopyroxene in the IBC component (Figures 1 and 5b; Table 1). Hence, we propose that a small but significant amount (between 2 and 5 wt%) of plagioclase definitely needs to be present in the lunar mantle cumulates at the depth of melting.

4.2. Melting a Lunar Hybridized Cumulate Mantle: What Are the Main Controls on Melt Composition?

Our experiments show that simple one-stage partial melting of a hybrid lunar cumulate mantle can produce melts with TiO_2 contents between 7 and 20 wt% that are very similar to the Apollo high-Ti pyroclastic glasses (Figure 4a). The experimental quenched melts are in equilibrium with olivine or olivine + orthopyroxene (Tables 2 and 3; e.g., Delano, 1980; Elkins et al., 2000; Krawczynski & Grove, 2012). In our experiments, no other phase is present near the liquidus P-T conditions. Spinel and ilmenite, however, appear at lower P-T (0.8 GPa, 1,320–1,250°C) in experiments GPC 785 and GPS 772, underlining the fact that ilmenite saturation is sensitive to pressure and temperature. The pressure in most of our experiments (1.5 GPa) corresponds to the shallower end of the predicted depth of the lunar basalt source (150–700 km depth; Delano, 1980; Elkins-Tanton et al., 2003). Experiments conducted at higher pressures (2.5 GPa, run ID GPC784) show the same phase relations as the run at 1.5 GPa (run ID GPC 769) and therefore we conclude that pressure has only a minor effect on the phase relations within the lunar mantle at the source depth of lunar basalts (Elkins-Tanton et al., 2002, and ref. therein), and that bulk mantle composition and temperature predominantly control the compositions of quenched melts in our study. Overall, the experimental results show that small-scale inhomogeneities in the lunar mantle significantly affect partial melt compositions.

In our experimental melts, the ol/opx of the starting material controls Mg# of the experimental melts, that is, starting materials with ol/opx > 1 best reproduce the lunar pyroclastic range and the ideal ol/opx of the starting material for reproducing Mg# of pyroclastic glasses is 1.2–1.5 (Figure 5a). A ratio of ol/cpx of 3/1 at low degrees of melting (i.e., 1,300°C) yields glass compositions that are similar in Mg# to the pyroclastic glasses (Figure 5b), whereas at high degrees of melting (red diamonds), the trend is opposite, with ol/cpx of 4/1–5/1 in the starting material yields quenched melts with Mg# similar to lunar pyroclastics. Al_2O_3/CaO and Mg# of the experimental glasses are very sensitive to the presence of orthopyroxene (Figures 2–5). Orthopyroxene in the experiments is very close to pure enstatite, but it does contain up to 3 mol% of wollastonite component (Table 3). Consequently, when orthopyroxene crystallizes, Al_2O_3/CaO in the glass decreases (Figures 4 and 5).

In summary, our experiments suggest that some plagioclase and Fe-Ti oxides must be present in the source of the picritic lunar basalts, if they are indeed a product of simple melting of a hybrid lunar cumulate. It is well established that plagioclase crystallizes when the LMO has solidified by 74%–80% and it continues to crystallize until the solidification is complete (Rapp & Draper, 2018; Schmidt & Kraettli, 2022). Fe-Ti oxides crystallize in the last ~5% of solidification together with plagioclase and clinopyroxene, hence we consider it very likely that small amounts of plagioclase were trapped between these mineral cumulates (Charlier et al., 2018; Dygert et al., 2017; Namur et al., 2011). A gravitational overturn after solidification of the LMO may then transport ilmenite, clinopyroxene, and small amounts of plagioclase into the deeper parts of the lunar mantle (e.g.,

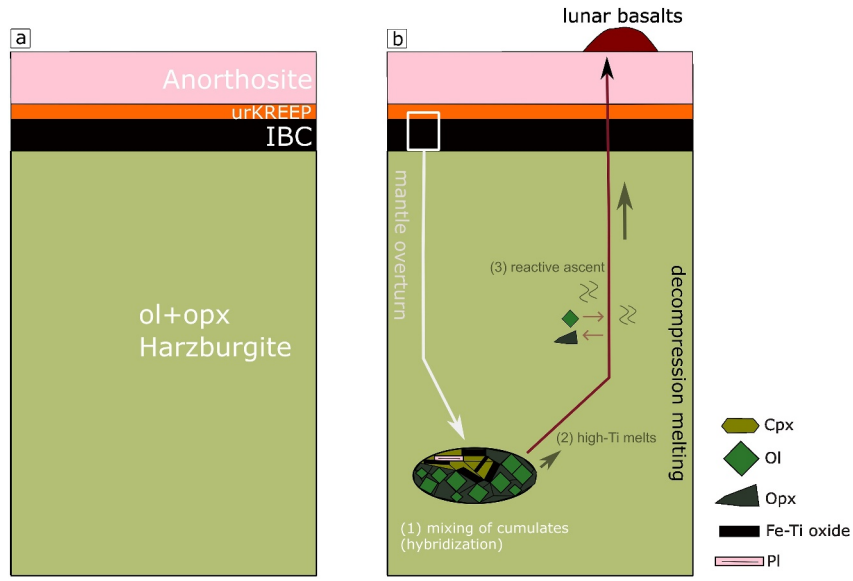

Figure 6. Sketch illustrating the formation of lunar basalts from a hybridized cumulate mantle as a consequence of a gravitationally driven overturn. (a) Crystallization of the lunar magma ocean leads to a solidified layered lunar mantle, where the anorthosite crust was formed by plagioclase flotation. A dense IBC layer rests on top of a harzburgite mantle and the urKREEP layer is wedged between the IBC and anorthosite crust (b) The high density of the IBC causes a large-scale mantle overturn and IBC (±urKREEP and plagioclase) is transported into the deep lunar mantle and hybridized along the way (1). Melting is caused mainly by decompression (2) high-Ti melts originate from single stage melting (see text). Partial melts from a heterogeneous mantle (ol + opx + cpx + ilm ± pl/urKREEP) with variable ilm/cpx cover the entire Ti range of the lunar high-Ti pyroclastic glasses. The melts will react with the host-rock during their ascent (3), altering their major and trace elemental budget and isotopic composition.

Ringwood & Kesson, 1976). These cumulates will then be mixed with harzburgite cumulate (Figure 6), and melting will occur mainly due to decompression of this mixed lithology, probably around the depth of multiple phase saturation.

Despite the similarities between our experimental data and the natural samples, we also see strong mismatches in TiO_2-CaO fractionation trend. Similar to Singletary and Grove (2008), we observe a positive correlation between TiO_2 and CaO parallel to their observed fractionation trend with modal proportions of ilmenite in the IBC layer (Figure 4b). Hence, we conclude that their suggestion that in a simple melting process the success of attaining high-Ti red and red-black lunar pyroclastic glass compositions is indeed controlled by the composition of the IBC layer. The proportion of ilm/cpx will influence the Ti content in the melt as will the degree of melting. High Ti-glasses in our experiments were attained by ilm/cpx between 4/5 and 4/1. CaO contents between 6 and 8 wt% were achieved, where ilm/cpx was 1/1 and 2/1 in compositions without added urKREEEP material and low degrees of melting. The composition CMV, which contained significant amounts of urKREEP component, also yielded appropriate CaO with very high degrees of melting (around 0.6). The yellow and orange pyroclastic glass compositions (TiO_2 between 3 and 10 wt%) which contain CaO comparable to the red pyroclastic glasses are not matched by our experiments, but experimental evidence has shown, that these compositions were approached by melting hybrid lunar mantle compositions with modal ilm/cpx (Brown & Grove, 2015; Singletary & Grove, 2008). Hence, we assume that simple melting process including IBC with variable ilm/cpx can be responsible for the variability in TiO_2 contents of the lunar pyroclastic glass suite from yellow to red.

However, there are several mismatches between our data and the natural samples, especially regarding Mg#, MgO/SiO_2, and Al_2O_3. We suggest that secondary processes after melting have affected the melt compositions. Depending on the density structure of the lunar interior, high-Ti melts were buoyant, rose up, or sunk to greater depth (Xu et al., 2022). Seismic data from the Moon indicates a deep molten layer within the lunar mantle, which has been interpreted as a remnant of the IBC, which upon overturn sunk to the core-mantle boundary (Mallik et al., 2019; Xu et al., 2022; Zhang et al., 2013, 2022). However, the same studies have emphasized that melts of a heterogeneous lunar mantle can be positively buoyant under certain circumstances. The overturn will not have

been completely efficient, leaving a significant proportion of IBC within the depth range of the origin of mare magmas (Xu et al., 2022). Hence, we assume that buoyant high-Ti melts ascended toward the lunar surface, potentially reacting with their surrounding host rock ("reactive ascent" Mallik et al., 2019). The major and trace element budget was altered by assimilation. In this study, we experimentally investigated a simple melting process, but experiments have shown that the interaction between a dunite mantle and an IBC layer at depth is complex (e.g., Scholpp & Dygert, 2024). Due to different solidus temperatures, the IBC layer will melt before the surrounding mantle starts to assimilate its host rock. Reaction-couple experiments by Scholpp and Dygert (2024) have shown that the olivine-undersaturated character of an IBC melt will enhance the dissolution of a dunite mantle, potentially further increasing the MgO content (and Mg#) of the melt. Additionally, clinopyroxene and garnet form as products of the assimilation. Fractionation of clinopyroxene lowers the SiO_2 and CaO contents, simultaneously enriching the melt in FeO and TiO_2. This process happens comparatively fast (within hours, see experiments in Klaver et al., 2024; Scholpp & Dygert, 2024). The modification of melts during reactive ascent has also been supported by reaction experiments using IBC melts and olivine + orthopyroxene (Klaver et al., 2024). The experiments showed, that during solid-liquid interaction of an IBC with a harzburgitic mineral assemblage, the minerals will be depleted in MgO. The Al_2O_3 of the melts rises due to an in situ replacement reaction of orthopyroxene, which scavenges the Al_2O_3 from the orthopyroxene, rendering the reacted melts more similar to high-Ti pyroclastic compositions in their Al_2O_3/CaO (Klaver et al., 2024). Melting of a hybrid lunar mantle and reactive ascent of these melts can further account for the high-Ti melt's Mg, Ca, Fe, and Ti isotopic signature (Klaver et al., 2024; K. B. Prissel et al., 2024). Hence, we propose that the process responsible for the chemical variety of the suite of lunar pyroclastic glasses (yellow to red-black) is a combination of melting a hybrid cumulate mantle and the reactive ascent of the melts.

4.3. Effects of an urKREEP Component in the Starting Material on Experimental Melt Compositions and the Origin of Low-Ti, High-Al Mare Basalts

Experimental quenched melts from starting materials containing an urKREEP major element component and low ilm/cpx (1/7) are very similar to low-Ti, high-Al mare basalts (Figures 4 and 5). The fraction of urKREEP we added is relatively high (0.3–0.4; Figure 1), but it should be noted that previous studies suggested no less than 15% of the KREEP component in the source of the high-Al and low-Ti mare basalts (Neal & Taylor, 1992; Neal et al., 1989). We produced melts similar to the high-Al basalt composition by melting a hybrid lunar mantle. Our experimental findings are a valuable contribution to the discussion on the origin of high-Al basalts. Similar to the high-Ti lunar basalts, it has been discussed if the low-Ti and high-Al basalts are the result of assimilation-fractional crystallization (S. Li et al., 2016; Neal & Taylor, 1992; Nyquist & Shih, 1992) or if these basalts are the product of melting of a hybrid lunar mantle (Hughes et al., 1990). Our experiments provide evidence that melting a hybrid lunar mantle containing significant proportions of an urKREEP major element component can produce melts similar to the high-Al basalts and support the feasibility of the latter hypothesis. This origin was also proposed based on the variability of incompatible trace element concentrations in those basalts (Hughes et al., 1990) and Ge-abundances (Dickinson et al., 1989). The elevated abundance of incompatible trace elements in high-Al basalt samples (especially A14 high-Al basalts) strongly supports the presence of urKREEP in their source (Hagerty et al., 2006; Hallis et al., 2014; Hui et al., 2013; S. Li et al., 2016). The question remains if the trace elemental signatures in natural lunar rocks correspond to the amounts of urKREEP component added as a major component in our starting materials. Trace element analyzes on natural lunar pyroclastic glasses have shown that they are variable and generally support the incorporation of a REE-enriched component, such as KREEP, in their source (Hagerty et al., 2006; Shearer & Papike, 1993). Nevertheless, the trace element abundances in the melt will be influenced by reactive ascent (see discussion above) and are also heavily dependent on eventual trapped liquids. It is hard to determine if the REE signatures of lunar basalts were inherited from the source, or if they were the product of assimilation (e.g., Münker, 2010). Final constraints on KREEP, its storage, its role in the overturn, and on its definite major element composition remain elusive.

Significant proportions of KREEP as a major component in the lunar mantle (0–50 wt%) can depress the melting points of lunar cumulates and could enhance the melt production by 2–13 times (Elardo et al., 2020). This could be a valuable contribution to produce significant amounts of melting on the Moon over a protracted time episode. The high-Al lunar basalts are relatively old (4.3–4 Ga; Nyquist & Shih, 1992) and were thought to be associated with lunar crustal rocks (e.g., Mg-suite rocks, Shearer & Papike, 1999). However, the presence of KREEP during

the emergence of Mg suite rocks has been debated and our experimental results underline that at least for explaining the major element characteristics in high-Ti lunar basalts, KREEP is not required.

On the contrary, our experiments suggest that a KREEP major element component is required in the source of early low-Ti, high-Al mare basalts. If the trace element signature of these basalts is primary, the observed variable enrichment of incompatible elements in the natural high-Al basalts indicates a heterogeneous source, such as a hybrid lunar mantle. It could also simulate different degrees of assimilation of the host rock. Assuming KREEP was overturned with the IBC layer, this component lowered the solidus, leading to an increased magma production and secondary crust building. This thickened crust could have acted as insulation on the lunar nearside, potentially limiting the amount of heat escape (Elardo et al., 2020; Laneuville et al., 2018). The concentration of KREEP in the lunar nearside mantle, possibly beneath the Procellarum KREEP Terrain (PKT), in conjunction with an insulating thick crust and heat coming from the cooling lunar core and core-mantle friction, provides a plausible explanation for long-lasting volcanic activity on the Moon (Haupt et al., 2023; Laneuville et al., 2018; Yu et al., 2023).

4.4. Implications for the Thermal Evolution of the Moon's Interior

Temperature constraints of our experiments indicate that significant lunar mantle melting occurred at the time of high-Al basalt emplacement and at the time of the eruption of high-Ti pyroclastic glasses (~4.0 and ~3.3–3.5 Ga ago; Delano, 1986; Papike et al., 1998; Snape et al., 2019). These observations are underlined by recent findings, suggesting that the transition between primary lunar crust (anorthosite layer) and secondary lunar crust (magmatic units, like Mg suite, KREEP basalts, mare basalts) began very early in lunar history and was indeed strongly controlled by the overturn of the mantle cumulates (T. C. Prissel et al., 2023). At least locally, significant melting in the lunar mantle will have occurred during a protracted period (Elardo et al., 2023). According to the melt fractions in our cumulate melting experiments, ~20%–40% degrees of melting are required to generate the observed variety of high-Ti lunar basalts. Melting of a solidified cumulate mantle occurs as a consequence of solid state convection inside solidified cumulates, possibly already taking place in lowermost cumulates, while the lunar magma ocean solidification was still not completed, relatively early in lunar history (Maurice et al., 2020; Morison et al., 2019). An overturn of relatively dense cumulates into a less dense underlying mantle will have induced upwellings, enforcing adiabatic decompression (Maurice et al., 2017, 2020). A gravitational overturn, a prerequisite assumption for our partial melting experiments, will enhance decompression melting by horizontal mass movement and thus enhance the melting of a hybrid, locally heterogeneous, lunar cumulate mantle (Figure 6). Significant melt fractions are produced by decompression mantle melting from e.g., 400 to 100 km depth (Hess, 1992; Ringwood & Kesson, 1976). Large-scale thermal inhomogeneities, as modeled for the Moon, may be responsible for rather local occurrences of lunar black and green picritic glass samples, which require a large degree of melting (30%–60%, Elkins-Tanton et al., 2003; Green & Ringwood, 1973; Solomon & Head, 1980; Wieczorek & Phillips, 2000; Zhang et al., 2022).

The overturn is driven by descending heavy ilmenite, clinopyroxene, and plagioclase-bearing (see discussion above) cumulates into the deeper mantle (H. Li et al., 2019; Yu et al., 2019), which consequently resulted in an upward movement of earlier and deeper harzburgite (Figure 6). We then envisage that the mantle harzburgite mixed with different amounts of the heavy cumulates, resulting in heterogeneous mixtures. Melting is caused mainly by decompression (Hess, 1992; Ringwood & Kesson, 1976). High-Ti lunar melts will be buoyant with respect to the lunar mantle, as long as they originate from a depth of about 250 km (Elkins-Tanton et al., 2002; Singletary & Grove, 2008; Xu et al., 2022), the depth of most of our experiments.

Our experiments give an idea on how a heterogeneous mantle on a local scale can influence melt compositions and our observations reinforce the IBC overturn model (Figure 6). However, a simple melting of our suggested hybrid lunar mantle compositions do not account for all major element systematics observed in lunar mantle melts and suggest that assimilation during reactive ascent is still required. Thus, our model proposes:

1. Mixing of the mantle cumulates due to overturn along the entire transect of their decent until melting occurs. A proportion of the IBC did not sink until the CMB. The overturn resulted in heterogeneous mantle cumulate compositions; this causes heterogeneities in the distribution of heat producing elements within the lunar mantle (Haupt, Renggli, Rohrbach, Berndt, Schwinger, et al., 2024).

2. Melting of the hybrid mantle occurs by decompression with additional heat provided by heat-producing elements and/or by impacts (Elkins-Tanton et al., 2004). Melting points might be decreased by plagioclase-rich KREEP material.
3. Ascending high-Ti melts were modified by assimilation during melt-rock interaction.

Accurate determination of the selenotherm is difficult due to the mantle heterogeneities (Wang et al., 2024). Consequently, we assume that the melting of the lunar mantle occurred in very localized regions, potentially toward lower pressures and depths, where melts are positively buoyant.

5. Conclusions

- Partial melting of a hybrid lunar mantle containing variable amounts of ilmenite bearing cumulate with nonmodal proportions of ilm/cpx/pl can generate melts that are similar to lunar high-Ti lunar pyroclastic glasses.
- Our results support the lunar magma ocean overturn model by which variable amounts of late stage cumulates rich in ilmenite and clinopyroxene with minor amounts of plagioclase can be transported into the lunar mantle.
- The suite of hybrid lunar mantle compositions, investigated in this study, does not account for all major element systematics in lunar pyroclastic glasses and calls for melt alteration during reactive ascent of these magmas, supporting evidence of incompatible trace elements and isotopic data.
- An urKREEP component in the source generates melts with a composition similar to the low-Ti and high-Al mare basalts. The heterogeneously distributed urKREEP component in the lunar mantle may also contribute significantly to the heat needed to generate lunar basalts much later than the overturn.

Conflict of Interest

The authors declare no conflicts of interest relevant to this study.

Data Availability Statement

The utilized data is represented within the publication and additional information is available from Haupt, Renggli, Rohrbach, Berndt, and Klemme (2024).

Acknowledgments
We thank the reviewers Stephen M. Elardo and an anonymous reviewer for their insightful comments, which have greatly improved this work. We further express our gratitude to the editor Bradley Thomson and AE Ananya Mallik for the suburban handling of the manuscript. This research was funded by the Deutsche Forschungsgemeinschaft (DFG) project 263649064—SFB TRR170, publication number 217. The authors are indebted to the workshops at Universität Münster for preparing the excellent piston cylinder assemblies, and our thanks also go to Maik Trogisch for his excellent job polishing the run products and to Beate Schmitte for her expert help with the EPMA. Data processing was done using python numpy, pandas and seaborn libraries. Open Access funding enabled and organized by Projekt DEAL.

References

Armstrong, J. T. (1991). Quantitative elemental analysis of individual microparticles with electron beam instruments. In K. F. J. Heinrich & D. E. Newbury (Eds.), *Electron probe quantitation* (pp. 261–315). Plenum Press.

Barr, J. A., & Grove, T. L. (2013). Experimental petrology of the Apollo 15 group A green glasses: Melting primordial lunar mantle and magma ocean cumulate assimilation. *Geochimica et Cosmochimica Acta*, *106*, 216–230. https://doi.org/10.1016/j.gca.2012.12.035

Bose, K., & Ganguly, J. (1995). Quartz-coesite transition revisited: Reversed experimental determination at 500–1200 C and retrieved thermochemical properties. *American Mineralogist*, *80*(3–4), 231–238. https://doi.org/10.2138/am-1995-3-404

Bottinga, Y., & Weill, D. F. (1970). Densities of liquid silicate systems calculated from partial molar volumes of oxide components. *American Journal of Science*, *269*(2), 169–182. https://doi.org/10.2475/ajs.269.2.169

Boyd, F. R., & England, J. L. (1960). Apparatus for phase-equilibrium measurements at pressures up to 50 kilobars and temperatures up to 1750°C. *Journal of Geophysical Research*, *65*(2), 741–748. https://doi.org/10.1029/JZ065i002p00741

Brown, S. M., & Grove, T. L. (2015). Origin of the Apollo 14, 15, and 17 yellow ultramafic glasses by mixing of deep cumulate remelts. *Geochimica et Cosmochimica Acta*, *171*, 201–215. https://doi.org/10.1016/j.gca.2015.09.001

Charlier, B., Grove, T. L., Namur, O., & Holtz, F. (2018). Crystallization of the lunar magma ocean and the primordial mantle-crust differentiation of the Moon. *Geochimica et Cosmochimica Acta*, *234*, 50–69. https://doi.org/10.1016/j.gca.2018.05.006

Delano, J. W. (1980). Chemistry and liquidus phase relations of Apollo 15 red glass: Implications for the deep lunar interior. In *Proceedings of the 11th Lunar and Planetary Science Conference* (pp. 251–288).

Delano, J. W. (1986). Pristine lunar glasses: Criteria, data, and implications. *Journal of Geophysical Research*, *91*(B4), 201–213. https://doi.org/10.1029/JB091iB04p0D201

Dickinson, T., Taylor, G. J., Keil, K., & Bild, R. W. (1989). Germanium abundances in lunar basalts-Evidence of mantle metasomatism? In *Proceedings of 19th Lunar and Planetary Science Conference* (pp. 189–198).

Dygert, N., Lin, J.-F., Marshall, E. W., Kono, Y., & Gardner, J. E. (2017). A low viscosity lunar magma ocean forms a stratified anorthitic flotation crust with mafic poor and rich units. *Geophysical Research Letters*, *44*(22), 11282–11291. https://doi.org/10.1002/2017GL075703

Elardo, S. M., Laneuville, M., McCubbin, F. M., & Shearer, C. K. (2020). Early crust building enhanced on the Moon's nearside by mantle melting-point depression. *Nature Geoscience*, *13*(5), 339–343. https://doi.org/10.1038/s41561-020-0559-4

Elardo, S. M., Pieters, C. M., Dhingra, D., Hanna, K. L. D., Glotch, T. D., Greenhagen, B. T., et al. (2023). The Evolution of the lunar crust. *Reviews in Mineralogy and Geochemistry*, *89*(1), 293–338. https://doi.org/10.2138/rmg.2023.89.07

Elkins, L. T., Fernandes, V. A., Delano, J. W., & Grove, T. L. (2000). Origin of lunar ultramafic green glasses: Constraints from phase equilibrium studies. *Geochimica et Cosmochimica Acta*, *64*(13), 2339–2350. https://doi.org/10.1016/S0016-7037(00)00365-3

Elkins-Tanton, L. T., Burgess, S., & Yin, Q.-Z. (2011). The lunar magma ocean: Reconciling the solidification process with lunar petrology and geochronology. *Earth and Planetary Science Letters*, *304*(3–4), 326–336. https://doi.org/10.1016/j.epsl.2011.02.004

Elkins-Tanton, L. T., Chatterjee, N., & Grove, T. L. (2003). Experimental and petrological constraints on lunar differentiation from the Apollo 15 green picritic glasses. *Meteoritics & Planetary Sciences*, *38*(4), 515–527. https://doi.org/10.1111/j.1945-5100.2003.tb00024.x

Elkins-Tanton, L. T., Hager, B. H., & Grove, T. L. (2004). Magmatic effects of the lunar late heavy bombardment. *Earth and Planetary Science Letters*, *222*(1), 17–27. https://doi.org/10.1016/j.epsl.2004.02.017

Elkins-Tanton, L. T., Van Orman, J. A., Hager, B. H., & Grove, T. L. (2002). Re-examination of the lunar magma ocean cumulate overturn hypothesis: Melting or mixing is required. *Earth and Planetary Science Letters*, *196*(3–4), 239–249. https://doi.org/10.1016/S0012-821X(01)00613-6

Fagan, T. J., Kashima, D., Wakabayashi, Y., & Suginohara, A. (2014). Case study of magmatic differentiation trends on the Moon based on lunar meteorite Northwest Africa 773 and comparison with Apollo 15 quartz monzodiorite. *Geochimica et Cosmochimica Acta*, *133*, 97–127. https://doi.org/10.1016/j.gca.2014.02.025

Finnila, A. B., Hess, P. C., & Rutherford, M. J. (1994). Assimilation by lunar mare basalts: Melting of crustal material and dissolution of anorthite. *Journal of Geophysical Research*, *99*(E7), 14677–14690. https://doi.org/10.1029/94JE01380

Fu, X., Yin, C., Jolliff, B. L., Zhang, J., Chen, J., Ling, Z., et al. (2022). Understanding the mineralogy and geochemistry of Chang'E-5 soil and implications for its geological significances. *Icarus*, *388*, 115254. https://doi.org/10.1016/j.icarus.2022.115254

Green, D. H., & Ringwood, A. E. (1973). Significance of a primitive lunar basaltic composition present in Apollo 15 soils and breccias. *Earth and Planetary Science Letters*, *19*(1), 1–8. https://doi.org/10.1016/0012-821X(73)90172-6

Green, D. H., Ringwood, A. E., Hibberson, W. O., & Ware, N. G. (1975). Experimental petrology of Apollo 17 mare basalts. In *Proceedings of the 6th Lunar and Planetary Science Conference* (pp. 871–893).

Guenther, M. E., Brown Krein, S. M., & Grove, T. L. (2022). The influence of variable oxygen fugacity on the source depths of lunar high-titanium ultramafic glasses. *Geochimica et Cosmochimica Acta*, *334*, 217–230. https://doi.org/10.1016/j.gca.2022.07.023

Hagerty, J. J., Shearer, C. K., & Vaniman, D. T. (2006). Heat-producing elements in the lunar mantle: Insights from ion microprobe analyses of lunar pyroclastic glasses. *Geochimica et Cosmochimica Acta*, *70*(13), 3457–3476. https://doi.org/10.1016/j.gca.2006.04.013

Hallis, L. J., Anand, M., & Strekopytov, S. (2014). Trace-element modelling of mare basalt parental melts: Implications for a heterogeneous lunar mantle. *Geochimica et Cosmochimica Acta*, *134*, 289–316. https://doi.org/10.1016/j.gca.2014.01.012

Haupt, C. P., Renggli, C. J., Klaver, M., Steenstra, E. S., Berndt, J., Rohrbach, A., & Klemme, S. (2023). Experimental and petrological investigations into the origin of the lunar Chang'E 5 basalts. *Icarus*, *402*, 115625. https://doi.org/10.1016/j.icarus.2023.115625

Haupt, C. P., Renggli, C. J., Rohrbach, A., Berndt, J., & Klemme, S. (2024). Replication Data for: Experimental constraints on the origin of the lunar high-Ti basalts [Dataset]. TRR170-DB. https://doi.org/10.35003/6CRMU9

Haupt, C. P., Renggli, C. J., Rohrbach, A., Berndt, J., Schwinger, S., Maurice, M., et al. (2024). Trace element partitioning in the lunar magma ocean: An experimental study. *Contributions to Mineralogy and Petrology*, *179*(5), 45. https://doi.org/10.1007/s00410-024-02118-z

Hess, P. C. (1992). Phase equilibria constraints on the origin of ocean floor basalts. *Washington DC American Geophysical Union Geophysical Monograph Series*, *71*, 67–102. https://doi.org/10.1029/gm071p0067

Hess, P. C., & Parmentier, E. M. (1995). A model for the thermal and chemical evolution of the Moon's interior: Implications for the onset of mare volcanism. *Earth and Planetary Science Letters*, *134*(3–4), 501–514. https://doi.org/10.1016/0012-821X(95)00138-3

Holloway, J. R., Pan, V., & Gudmundsson, G. (1992). High-pressure fluid-absent melting experiments in the presence of graphite: Oxygen fugacity, ferric/ferrous ratio and dissolved CO_2. *European Journal of Mineralogy*, *4*(1), 105–114. https://doi.org/10.1127/ejm/4/1/0105

Hubbard, N. J., & Minear, J. W. (1975). A chemical and physical model for the genesis of lunar rocks: Part II mare basalts. In *Proceedings of the 6th Lunar and Planetary Science Conference* (Vol. 405). Retrieved from https://adsabs.harvard.edu/full/1975LPI…6..405H

Hughes, S. S., Neal, C. R., & Taylor, L. A. (1990). Petrogenesis of Apollo 14 high (HA) parental basaltic magma. In *Proceedings of the 21st Lunar and Planetary Science Conference* (Vol. 540).

Hui, H., Neal, C. R., Shih, C.-Y., & Nyquist, L. E. (2013). Petrogenetic association of the oldest lunar basalts: Combined Rb–Sr isotopic and trace element constraints. *Earth and Planetary Science Letters*, *373*, 150–159. https://doi.org/10.1016/j.epsl.2013.04.034

Khan, A., Connolly, J. A. D., Pommier, A., & Noir, J. (2014). Geophysical evidence for melt in the deep lunar interior and implications for lunar evolution. *Journal of Geophysical Research: Planets*, *119*(10), 2197–2221. https://doi.org/10.1002/2014JE004661

Klaver, M., Klemme, S., Liu, X.-N., Hin, R. C., Coath, C. D., Anand, M., et al. (2024). Titanium-rich basaltic melts on the Moon modulated by reactive flow processes. *Nature Geoscience*, *17*(2), 118–123. https://doi.org/10.1038/s41561-023-01362-5

Klemme, S., & O'Neill, H. S. (1997). The reaction $MgCr_2O_4 + SiO_2 = Cr_2O_3 + MgSiO_3$ and the free energy of formation of magnesiochromite ($MgCr_2O_4$). *Contributions to Mineralogy and Petrology*, *130*(1), 59–65. https://doi.org/10.1007/s004100050349

Kommescher, S., Fonseca, R. O., Kurzweil, F., Thiemens, M. M., Münker, C., & Sprung, P. (2020). Unravelling lunar mantle source processes via the Ti isotope composition of lunar basalts. *Geochemical Perspective Letters*, *13*, 13–18. https://doi.org/10.7185/geochemlet.2007

Krawczynski, M. J., & Grove, T. L. (2012). Experimental investigation of the influence of oxygen fugacity on the source depths for high titanium lunar ultramafic magmas. *Geochimica et Cosmochimica Acta*, *79*, 1–19. https://doi.org/10.1016/j.gca.2011.10.043

Laneuville, M., Taylor, J., & Wieczorek, M. A. (2018). Distribution of radioactive Heat sources and thermal history of the Moon. *Journal of Geophysical Research: Planets*, *123*(12), 3144–3166. https://doi.org/10.1029/2018JE005742

Laneuville, M., Wieczorek, M. A., Breuer, D., & Tosi, N. (2013). Asymmetric thermal evolution of the Moon. *Journal of Geophysical Research: Planets*, *118*(7), 1435–1452. https://doi.org/10.1002/jgre.20103

Li, H., Zhang, N., Liang, Y., Wu, B., Dygert, N. J., Huang, J., & Parmentier, E. M. (2019). Lunar cumulate mantle overturn: A model constrained by ilmenite rheology. *Journal of Geophysical Research: Planets*, *124*(5), 1357–1378. https://doi.org/10.1029/2018JE005905

Li, S., Hsu, W., Guan, Y., Wang, L., & Wang, Y. (2016). Petrogenesis of the Northwest Africa 4898 high-Al mare basalt. *Meteoritics & Planetary Sciences*, *51*(7), 1268–1288. https://doi.org/10.1111/maps.12663

Longhi, J. (1992). Experimental petrology and petrogenesis of mare volcanics. *Geochimica et Cosmochimica Acta*, *56*(6), 2235–2251. https://doi.org/10.1016/0016-7037(92)90186-M

Longhi, J. (2006). Petrogenesis of picritic mare magmas: Constraints on the extent of early lunar differentiation. *Geochimica et Cosmochimica Acta*, *70*(24), 5919–5934. https://doi.org/10.1016/j.gca.2006.09.023

Mallik, A., Ejaz, T., Shcheka, S., & Garapic, G. (2019). A petrologic study on the effect of mantle overturn: Implications for evolution of the lunar interior. *Geochimica et Cosmochimica Acta*, *250*, 238–250. https://doi.org/10.1016/j.gca.2019.02.014

Maurice, M., Tosi, N., Samuel, H., Plesa, A., Hüttig, C., & Breuer, D. (2017). Onset of solid-state mantle convection and mixing during magma ocean solidification. *Journal of Geophysical Research: Planets*, *122*(3), 577–598. https://doi.org/10.1002/2016JE005250

Maurice, M., Tosi, N., Schwinger, S., Breuer, D., & Kleine, T. (2020). A long-lived magma ocean on a young Moon. *Science Advances*, *6*(28), eaba8949. https://doi.org/10.1126/sciadv.aba8949

McCallum, I. S., Raedeke, L. D., & Mathez, E. A. (1980). Investigations of the stillwater complex: Part I. Stratigraphy and structure of the banded zone. *American Journal of Science*, *280*(1), 59–87.

Medard, E., McCammon, C. A., Barr, J. A., & Grove, T. L. (2008). Oxygen fugacity, temperature reproducibility, and H_2O contents of nominally anhydrous piston-cylinder experiments using graphite capsules. *American Mineralogist*, *93*(11–12), 1838–1844. https://doi.org/10.2138/am.2008.2842

Morison, A., Labrosse, S., Deguen, R., & Alboussière, T. (2019). Timescale of overturn in a magma ocean cumulate. *Earth and Planetary Science Letters*, *516*, 25–36. https://doi.org/10.1016/j.epsl.2019.03.037

Münker, C. (2010). A high field strength element perspective on early lunar differentiation. *Geochimica et Cosmochimica Acta*, *74*(24), 7340–7361. https://doi.org/10.1016/j.gca.2010.09.021

Namur, O., Charlier, B., Pirard, C., Hermann, J., Liégeois, J.-P., & Auwera, J. V. (2011). Anorthosite formation by plagioclase flotation in ferrobasalt and implications for the lunar crust. *Geochimica et Cosmochimica Acta*, *75*(17), 4998–5018. https://doi.org/10.1016/j.gca.2011.06.013

Neal, C. R., & Taylor, L. A. (1992). Petrogenesis of mare basalts: A record of lunar volcanism. *Geochimica et Cosmochimica Acta*, *56*(6), 2177–2211. https://doi.org/10.1016/0016-7037(92)90184-K

Neal, C. R., Taylor, L. A., Schmitt, R. A., Hughes, S. S., & Lindstrom, M. M. (1989). High alumina (HA) and very high potassium (VHK) basalt clasts from Apollo 14 breccias. II-Whole rock geochemistry-Further evidence for combined assimilation and fractional crystallization within the lunar crust. In *Proceedings of the 19th Lunar and Planetary Science Conference* (pp. 147–161).

Nicholis, M. G., & Rutherford, M. J. (2009). Graphite oxidation in the Apollo 17 orange glass magma: Implications for the generation of a lunar volcanic gas phase. *Geochimica et Cosmochimica Acta*, *73*(19), 5905–5917. https://doi.org/10.1016/j.gca.2009.06.022

Nyquist, L. E., & Shih, C.-Y. (1992). The isotopic record of lunar volcanism. *Geochimica et Cosmochimica Acta*, *56*(6), 2213–2234. https://doi.org/10.1016/0016-7037(92)90185-L

Papike, J. J., Fowler, G. W., & Shearer, C. K. (1997). Evolution of the lunar crust: SIMS study of plagioclase from ferroan anorthosites. *Geochimica et Cosmochimica Acta*, *61*(11), 2343–2350. https://doi.org/10.1016/S0016-7037(97)00086-0

Papike, J. J., Ryder, G., & Shearer, C. K. (1998). Lunar samples. In *Planetary materials* (Vol. 36, pp. 5-1–234). Mineralogical Society of America.

Papike, J. J., & Vaniman, D. T. (1978). Luna 24 ferrobasalts and the mare basalt suite: Comparative chemistry, mineralogy, and petrology. In *Mare Crisium: The view from Luna 24* (pp. 371–401).

Prissel, K. B., Krawczynski, M. J., Nie, N. X., Dauphas, N., Aarons, S. M., Heard, A. W., et al. (2024). Fractionation of iron and titanium isotopes by ilmenite and the isotopic compositions of lunar magma ocean cumulates. *Geochimica et Cosmochimica Acta*, *372*, 154–170. https://doi.org/10.1016/j.gca.2024.01.006

Prissel, T. C., Zhang, N., Jackson, C. R. M., & Li, H. (2023). Rapid transition from primary to secondary crust building on the Moon explained by mantle overturn. *Nature Communications*, *14*(1), 5002. https://doi.org/10.1038/s41467-023-40751-7

Rapp, J. F., & Draper, D. S. (2018). Fractional crystallization of the lunar magma ocean: Updating the dominant paradigm. *Meteoritics & Planetary Sciences*, *53*(7), 1432–1455. https://doi.org/10.1111/maps.13086

Ringwood, A. E., & Essene, E. (1970). Petrogenesis of lunar basalts and the internal constitution and origin of the Moon. *Science*, *167*(3918), 607–610. https://doi.org/10.1126/science.167.3918.607

Ringwood, A. E., Green, D. H., & Ware, N. G. (1972). Experimental petrology and petrogenesis of Apollo 14 basalts. In *Proceedings of the 3rd Lunar and Planetary Science Conference* (pp. 197–206).

Ringwood, A. E., & Kesson, S. E. (1976). A dynamic model for mare basalt petrogenesis. In *Proceedings of the 7th Lunar and Planetary Science Conference* (pp. 1697–1722).

Sato, M., Hickling, N. L., & McLane, J. W. (1973). Oxygen fugacity values of Apollo 12, 14 and 15 lunar samples and reduced state of lunar magmas. In *Proceedings of the 4th Lunar Science Conference* (pp. 1061–1079).

Schmidt, M. W., & Kraettli, G. (2022). Experimental crystallization of the lunar magma ocean, initial selenotherm and density stratification, and implications for crust formation, overturn and the bulk silicate Moon composition. *Journal of Geophysical Research: Planets*, *127*(5), e2022JE007187. https://doi.org/10.1029/2022JE007187

Scholpp, J. L., & Dygert, N. (2024). Experimental insights into the mineralogy and melt-rock reactions produced by lunar cumulate mantle overturn. *Contributions to Mineralogy and Petrology*, *179*(6), 58. https://doi.org/10.1007/s00410-024-02134-z

Shearer, C. K., Hess, P. C., Wieczorek, M. A., Pritchard, M. E., Parmentier, E. M., Borg, L. E., et al. (2006). Thermal and magmatic evolution of the Moon. *Reviews in Mineralogy and Geochemistry*, *60*(1), 365–518. https://doi.org/10.2138/rmg.2006.60.4

Shearer, C. K., & Papike, J. J. (1993). Basaltic magmatism on the Moon: A perspective from volcanic picritic glass beads. *Geochimica et Cosmochimica Acta*, *57*(19), 4785–4812. https://doi.org/10.1016/0016-7037(93)90200-G

Shearer, C. K., & Papike, J. J. (1999). Magmatic evolution of the Moon. *American Mineralogist*, *84*(10), 1469–1494. https://doi.org/10.2138/am-1999-1001

Shearer, C. K., Papike, J. J., Galbreath, K. C., & Shimizu, N. (1991). Exploring the lunar mantle with secondary ion mass spectrometry: A comparison of lunar picritic glass beads from the Apollo 14 and Apollo 17 sites. *Earth and Planetary Science Letters*, *102*(2), 134–147. https://doi.org/10.1016/0012-821X(91)90003-Z

Singletary, S., & Grove, T. (2008). Origin of lunar high-titanium ultramafic glasses: A hybridized source? *Earth and Planetary Science Letters*, *268*(1–2), 182–189. https://doi.org/10.1016/j.epsl.2008.01.019

Snape, J. F., Nemchin, A. A., Whitehouse, M. J., Merle, R. E., Hopkinson, T., & Anand, M. (2019). The timing of basaltic volcanism at the Apollo landing sites. *Geochimica et Cosmochimica Acta*, *266*, 29–53. https://doi.org/10.1016/j.gca.2019.07.042

Snyder, G. A., Taylor, L. A., & Neal, C. R. (1992). A chemical model for generating the sources of mare basalts: Combined equilibrium and fractional crystallization of the lunar magmasphere. *Geochimica et Cosmochimica Acta*, *56*(10), 3809–3823. https://doi.org/10.1016/0016-7037(92)90172-F

Solomon, S. C., & Head, J. W. (1980). Lunar Mascon Basins: Lava filling, tectonics, and evolution of the lithosphere. *Reviews of Geophysics*, *18*(1), 107–141. https://doi.org/10.1029/RG018i001p00107

Solomon, S. C., & Nafi Toksöz, M. (1973). Internal constitution and evolution of the moon. *Physics of the Earth and Planetary Interiors*, *7*(1), 15–38. https://doi.org/10.1016/0031-9201(73)90037-X

Spera, F. J. (1992). Lunar magma transport phenomena. *Geochimica et Cosmochimica Acta*, *56*(6), 2253–2265. https://doi.org/10.1016/0016-7037(92)90187-N

Thacker, C., Liang, Y., Peng, Q., & Hess, P. (2009). The stability and major element partitioning of ilmenite and armalcolite during lunar cumulate mantle overturn. *Geochimica et Cosmochimica Acta*, *73*(3), 820–836. https://doi.org/10.1016/j.gca.2008.10.038

van Kan Parker, M., Mason, P. R. D., & van Westrenen, W. (2011). Trace element partitioning between ilmenite, armalcolite and anhydrous silicate melt: Implications for the formation of lunar high-Ti mare basalts. *Geochimica et Cosmochimica Acta*, *75*(15), 4179–4193. https://doi.org/10.1016/j.gca.2011.04.031

Van Orman, J. A., & Grove, T. L. (2000). Origin of lunar high-titanium ultramafic glasses: Constraints from phase relations and dissolution kinetics of clinopyroxene-ilmenite cumulates. *Meteoritics & Planetary Sciences*, *35*(4), 783–794. https://doi.org/10.1111/j.1945-5100.2000.tb01462.x

Wagner, T. P., & Grove, T. L. (1997). Experimental constraints on the origin of lunar high-Ti ultramafic glasses. *Geochimica et Cosmochimica Acta*, *61*(6), 1315–1327. https://doi.org/10.1016/S0016-7037(96)00387-0

Wang, C., Xu, Y.-G., Zhang, L., Chen, Z., Xia, X., Lin, M., & Guo, F. (2024). A shallow (<100 km) ilmenite-bearing pyroxenitic source for young lunar volcanism. *Earth and Planetary Science Letters*, *639*, 118770. https://doi.org/10.1016/j.epsl.2024.118770

Warren, P. H. (1985). The magma ocean concept and lunar evolution. *Annual Review of Earth and Planetary Sciences*, *13*(1), 201–240. https://doi.org/10.1146/annurev.ea.13.050185.001221

Warren, P. H., & Wasson, J. T. (1979). The origin of KREEP. *Reviews of Geophysics*, *17*(1), 73–88. https://doi.org/10.1029/RG017i001p00073

Weitz, C. M., Rutherford, M. J., & Head, J. W. (1997). Oxidation states and ascent history of the Apollo 17 volcanic beads as inferred from metal-glass equilibria. *Geochimica et Cosmochimica Acta*, *61*(13), 2765–2775. https://doi.org/10.1016/S0016-7037(97)00119-1

Wieczorek, M. A., & Phillips, R. J. (2000). The "Procellarum KREEP Terrane": Implications for mare volcanism and lunar evolution. *Journal of Geophysical Research*, *105*(E8), 20417–20430. https://doi.org/10.1029/1999JE001092

Wieczorek, M. A., Shearer, C. K., & Neal, C. R. (2006). In B. L. Jolliff (Ed.), *New views of the Moon* (Vol. 60). Mineralogical Society of America.

Xirouchakis, D., Hirschmann, M. M., & Simpson, J. A. (2001). The effect of titanium on the silica content and on mineral-liquid partitioning of mantle-equilibrated melts. *Geochimica et Cosmochimica Acta*, *65*(14), 2201–2217. https://doi.org/10.1016/S0016-7037(00)00549-4

Xu, M., Jing, Z., Van Orman, J. A., Yu, T., & Wang, Y. (2022). Experimental evidence supporting an overturned iron-titanium-rich melt layer in the deep lunar interior. *Geophysical Research Letters*, *49*(13), e2022GL099066. https://doi.org/10.1029/2022GL099066

Yu, S., Tosi, N., Schwinger, S., Maurice, M., Breuer, D., & Xiao, L. (2019). Overturn of ilmenite-bearing cumulates in a rheologically weak lunar mantle. *Journal of Geophysical Research: Planets*, *124*(2), 418–436. https://doi.org/10.1029/2018je005739

Yu, S., Xiao, X., Gong, S., Tosi, N., Huang, J., Breuer, D., et al. (2023). Long-lived lunar volcanism sustained by precession-driven core-mantle friction. *National Science Review*, *nwad276*(2). https://doi.org/10.1093/nsr/nwad276

Zhang, N., Ding, M., Zhu, M.-H., Li, H., Li, H., & Yue, Z. (2022). Lunar compositional asymmetry explained by mantle overturn following the South Pole–Aitken impact. *Nature Geoscience*, *15*(1), 37–41. https://doi.org/10.1038/s41561-021-00872-4

Zhang, N., Parmentier, E. M., & Liang, Y. (2013). A 3-D numerical study of the thermal evolution of the Moon after cumulate mantle overturn: The importance of rheology and core solidification. *Journal of Geophysical Research: Planets*, *118*(9), 1789–1804. https://doi.org/10.1002/jgre.20121